ORIGINAL PAPER

A Geomechanical Evaluation of Fault Reactivation Using Analytical Methods and Numerical Simulation

Majid Taghipour[1] · Mohammad Ghafoori[1] · Gholam Reza Lashkaripour[1] · Nasser Hafezi Moghaddas[1] · Abdullah Molaghab[2]

Abstract

One of the main problems related to mature oilfields is the decreased pore pressure due to hydrocarbon production. Therefore, to maintain the production rate of a reservoir, the lost pressure must be compensated. A very traditional method to increase the pressure is to inject natural gas into the reservoir. This technique is widely used in SW Iranian reservoirs because of the readily available supply of this type of gas. Reactivation of pre-existing faults and inducing new fractures into the reservoir and cap rock are some of the potential risks regarding gas injection. In this article, using data such as well logs, pore pressure estimates, and rock mechanical test results, the geomechanical simulation of the Asmari reservoir in the Gachsaran oilfield, SW Iran has been carried out. For this purpose, the current stress field was determined using elastic moduli of reservoir rocks and formation integrity test (FIT) results. Then, by applying analytical methods such as Mohr diagrams and slip tendency, the reactivation possibility of four faults in the field was analyzed, and the maximum sustainable pore pressures were estimated. In the next step, numerical simulations were conducted using ABAQUS software to investigate the injected gas flow path, leakage potential through the cap rock, possible fault reactivation due to gas injection, and shear stress build-up and plastic strain development in different parts of the reservoir. Results of Mohr diagrams and slip tendency showed that all the faults are stable in the current stress state, and fault F2 has the potential to sustain a maximum pore pressure of 55 MPa in the field. On the other hand, fault F3 has the proper conditions (i.e., strike and dip referring to σ_{Hmax} orientation) for reactivation. Results of numerical simulations suggested that an injection pressure of 30 MPa would not induce any new fracture or fault slip within 5 years of injection. In this period, the injected gas plume moves upward through the damage zone and reaches the shallower parts of the cap rock. It was also shown that by applying an injection pressure of 60 MPa, slip would occur on fault F4 after 10 days of injection.

Keywords Gachsaran oilfield · Asmari reservoir · Fault stability · Geomechanical modeling · Analytical methods · Numerical simulation

List of symbols

FIT	Formation integrity test
API	American Petroleum Institute gravity, °
c	Cohesion strength of rock, MPa
μ_s	Coefficient of static friction
$\sigma_1, \sigma_2, \sigma_3$	The maximum, the intermediate, and the minimum principal stresses, MPa
σ_V	Vertical stress, MPa
σ_{Hmax}	Maximum horizontal stress, MPa
σ_{hmin}	Minimum horizontal stress, MPa
ρ	Overburden density, kg/m^3
$\bar{\rho}$	Mean overburden density, kg/m^3
g	Gravitational acceleration, m/s^2
z	Depth, m
LOT	Leak-off test
XLOT	Extended leak-off test
LT	Limited test
LOP	Leak-off point
ν_s	Static Poisson's ratio
E_s	Static Young's modulus, GPa
P_P	Pore pressure, MPa
α	Biot's coefficient

✉ Majid Taghipour
Majidtaghipour1989@gmail.com

[1] Department of Geology, Faculty of Science, Ferdowsi University of Mashhad, Mashhad, Iran

[2] National Iranian South Oil Company (NISOC), Ahwaz, Iran

ε_x	Magnitude of the rock deformation in the x plane
ε_y	Magnitude of the rock deformation in the y plane
DST	Drill stem test
RFT	Repeat formation test
P_{pg}	Formation pressure gradient, MPa/m
P_{ng}	Hydrostatic pore pressure gradient, MPa/m
Δ_t	Measured sonic transit time by well logging, μs/ft
x	Exponent constant
S_g	Overburden pressure gradient, MPa/m
ρ_b	Bulk density of rock, kg/m^3
K	Permeability, mD
rfn	Rock fabric number
Φ_{ip}	Interparticle porosity
S_{wi}	Initial water saturation
PHIE	Effective porosity log
n, Φ	Porosity, %
PHIT	Total porosity log
ν_d	Dynamic Poisson's ratio
E_d	Dynamic Young's modulus, GPa
UCS	Uniaxial compressive strength, MPa
σ_t	Tensile strength, MPa
φ	Friction angle, °
NPHI	Neutron porosity
V_{sh}	Shale volume
θ	Angle between the normal to the fracture plane of and σ_1, °
GR	Gamma ray
σ_n	Normal stress, MPa
τ	Shear stress, MPa
$\beta1, \beta2, \beta3$	Angles between plane normal and the axes of σ_1, σ_2, and σ_3, °
Ts	Slip tendency
σ'_n	Effective normal stress, MPa
P_C	Critical pore pressure, MPa
q	Slope of the σ'_1 versus σ'_3 line
T_d	Dilation tendency
σ'_1, σ'_3	The maximum and the minimum effective principal stresses, MPa
k	Hydraulic conductivity, m/s
σ'_{ni}	Effective normal stress on the fault plane (prior to gas injection), MPa
P_{pi}	Initial pore pressure of the reservoir (prior to gas injection), MPa
P_{pmax}	The maximum sustainable pore pressure due to gas injection, MPa
σ'_{nf}	Effective normal stress at the failure point, MPa
ΔP_p	The maximum pore pressure increase needed for fault reactivation, MPa

1 Introduction

Gas injection is a common practice for maintaining reservoir pressure in mature oilfields. Hydrocarbon production will result in reduced pressure in the reservoir formation, and hydrocarbons will be replaced with other formation fluids (e.g., brines). Since the 1960s, it has been a regular practice to inject fluids into the reservoir to maintain the production rate (Verdon 2012).

Injection raises pore pressure in the target reservoir. This action reduces the effective stress, which causes the deformation of rocks. The amount of this geomechanical deformation is controlled by material properties of the formation and the magnitude of the pore pressure increase caused by the injection. The deformation may induce cap rock integrity issues. If pre-existing faults reactivate or new fractures develop, an escape path for injected gas will be introduced. Therefore, to ensure safe injection operations, it should be guaranteed that the deformation will not damage the cap rock. Zhang et al. (2006) demonstrated that gas leakage is due to hydraulic fracturing that is related to cap rock pressure increase or stress change in the system. As long as the reservoir pressure does not exceed the initial pressure of the formation, the risk of leakage through pre-existing fractures is low. Lithology and the structural setting of the reservoir and overburden are two significant factors that affect the gas migration through the cap rock.

Pre-existing faults and fractures in a reservoir may provide a conduit for leakage through fault reactivation. Therefore, investigations on the maximum sustainable injection pressure on sealing faults that act as structural traps are an integral part of geomechanical studies to ensure safe injection (Streit and Hillis 2004; Richey 2013). The initial sealing capacity of cap rocks may vanish by their reactivation (Wiprut and Zoback 2002; Gartrell et al. 2006; Langhi et al. 2010), which is induced by fluid injection into the reservoirs (Nicholson and Wesson 1990; Guha 2000; Cornet 2012; Evans et al. 2012; Keranen et al. 2013; McGarr et al. 2015).

Faults may assist the fluid flow at depth, based on the hypothesis of critically stressed faults. This hypothesis states that favorably oriented and critically stressed faults and fractures that are prone to frictional failure should control both fluid flow and reactivation potential (Barton et al. 1995; Sibson 1996; Ito and Zoback 2000; Ferrill et al. 2019). Increased pore pressure caused by injection may lead to shear slip failure of existing fractures when the maximum shear stress exceeds the shear strength. The resulting increase in fault roughness creates a potential leakage path, and thereby permeability enhancement. When an internally connected network of open fractures

forms, it can act as a migration conduit for gas-rich fluids along the rough surface of faults. Therefore, one of the most critical parts of any investigation for a potential gas injection site is analyzing the risk of fault reactivation. In any injection project, identifying and characterizing faults is crucial, because their stability can be dramatically affected. Faults generally cannot be avoided in compartmentalized reservoirs (Castelletto et al. 2013). Reservoir compartmentalization is the segregation of a petroleum reservoir into a number of individual fluid or pressure compartments by bounding features (e.g., impermeable faults) which prevent hydrocarbon crossflow (Caine et al. 1996). Thus, they can be a restricting agent (by creating over-pressured segments caused by gas injection) that can reduce the safe injection operation (Fig. 1). For example, the excessive overpressure induced by low permeability faults in Snøvit, Norway, halted CO_2 injection operations after a few months (Hansen et al. 2013). Therefore, to minimize the risk of fault reactivation, injection wells should be located as far as possible from faults and thus avoid limitations on the injection rate (Vilarrasa et al. 2016).

It is worth noting that even if fault reactivation does not lead to gas migration to the ground surface, such activities may reduce the sealing ability of nearby layers, which potentially lead to groundwater pollution.

We report in this paper the results of geomechanical modeling of the Asmari reservoir in the Gachsaran oilfield applied to an investigation of the potential for fault slippage and the creation of new fractures. The results of such studies can be used for locating safe injection points, identifying potential damage zones in the cap rock, and can be applied to the mitigation of other hazards related to gas injection with further geomechanical studies.

2 Geological Setting

The Gachsaran oilfield is an asymmetric anticline structure located in Dezful-Embayment in the vicinity of Ahvaz city (Fig. 2a). This field is situated in the Iranian section of Zagros fold-thrust belt, a belt that stretches from Anatolian fault in eastern Turkey to the Minab fault near the Makran region in the southeast of Iran. This fold-thrust belt is a part of an active foreland basin complex, which was initiated in the Late Tertiary time by the collision between Iranian and Arabian Plates (Stocklin 1974; Berberian and King 1981). This field is an elongated doubly-plunging anticlinal structure with dimensions of 65 km length and 4–8 km width and is considered one of the most significant productive oilfields in the Oligocene–Lower Miocene carbonate horizons (Shaban et al. 2011). The Cretaceous to Early Miocene petroleum system of the field includes two carbonate reservoirs: Asmari (Early Miocene) and Bangestan (including the Cenomanian–Turonian aged Sarvak formation and the
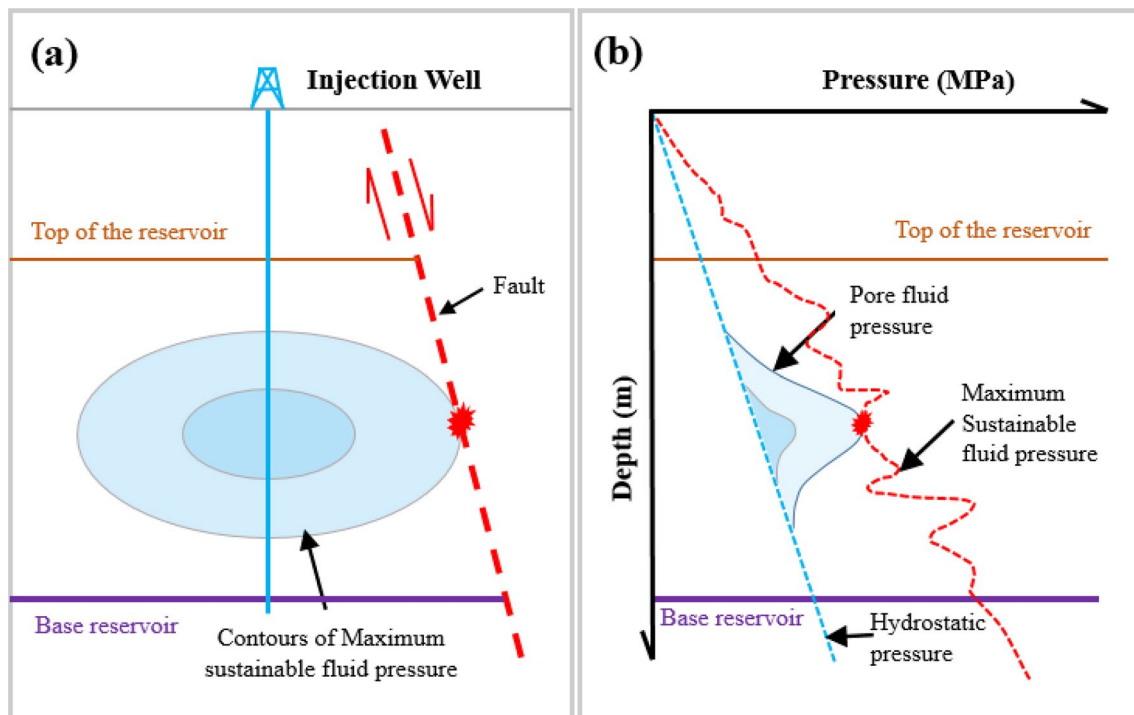
Fig. 1 **a** Schematic illustration of pore pressure contours after injection, and **b** pressure-depth plot showing the excessive overpressures caused by a low permeable fault (Meng et al. 2016)
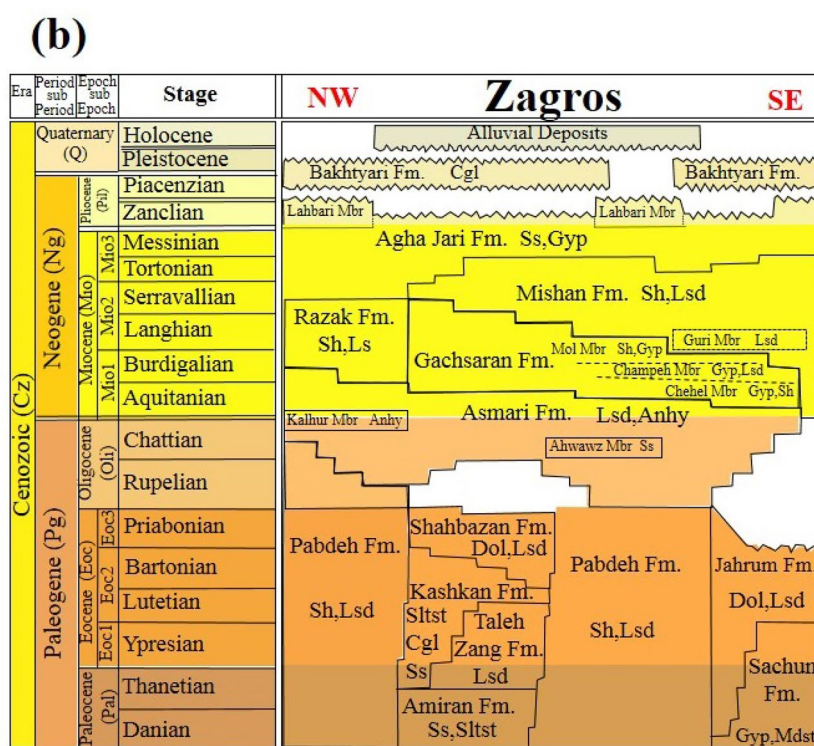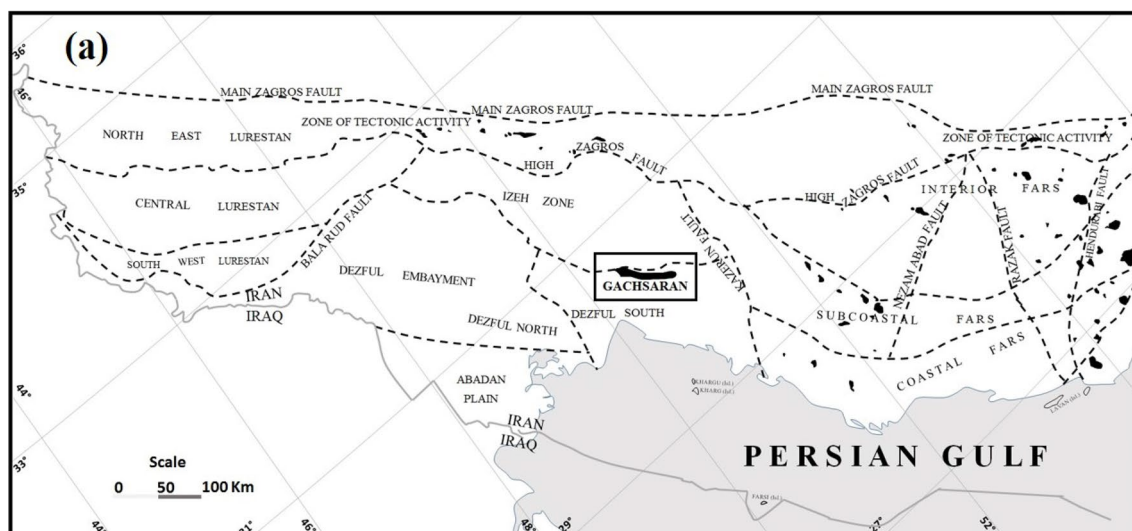
Fig. 2 **a** Location of Gachsaran oil filed in Zagros fold-thrust belt (Shaban et al. 2011), **b** stratigraphic column of the field (Geological Society of Iran, GSI 2018)

Santonian aged Ilam formation), which are sealed by the evaporitic Gachsaran (Miocene) and the marly Gurpi (Late Cretaceous) formations, respectively (Alizadeh et al. 2018).

The Asmari reservoir is one of the most well-known reservoirs in the world and produces almost 85% of total Iranian crude oil, which is characterized by its 30° API gravity and low sulfur content (Rezaie and Nogole-Sadat 2004). This reservoir was first discovered by the Anglo-Persian Oil Company in 1931 and had a peak production of 180 thousand

barrels per day in 1976. The Asmari formation consists of cream to gray limestone, dolomitic limestone, and dolomite, and its thickness in the type section is 314 m (Darvishzadeh 2009). The cap rock of this oilfield is a Miocene aged formation called Gachsaran formation, which consists of seven members. This formation is composed of anhydrite, limestone, and bituminous shale, and its oldest and lowermost member, which is the cap rock of the Asmari reservoir, is referred to as Member 1 (James and Wynd 1965). The

average thickness of Member 1 in this field is about 40 m (Darvishzadeh 2009). The lower contact of Asmari formation is the Pabdeh formation, which is the reservoir source rock with an age of Paleocene to Eocene. Figure 2b shows the Cenozoic era of the stratigraphic column in the Zagros fold-thrust belt.

In this study, we have investigated the stability of four faults of F1, F2, F3, and F4 located in the western sector of the field. Figure 3 shows the underground contour map of the faults and their cross section in the study area. All the faults are normal, and since there was no information about their cohesion (*c*) and friction coefficient (μ_s), these parameters were assumed to be zero and 0.6, respectively. Rock mechanics tests on a wide range of rocks have demonstrated that the coefficient of friction ranges between 0.6 and 1.0 (Byerlee 1978). A $\mu_s = 0.6$ is a lower boundary value and a conservative assumption used by many researchers who have investigated fault stability (e.g., Rutqvist et al. 2007; Zoback 2007; Konstantinovskaya et al. 2012; Figueiredo et al. 2015). Zero cohesion is a reasonable assumption given the fault has

already ruptured. The structural characteristics of the faults are summarized in Table 1.

3 Theory and Background

3.1 Introduction of Methodology

Generally, the first step in any geomechanical study is to identify the stress regime and the relationship among the three principal stresses. First, the static elastic moduli of the rocks were estimated using well logs and data obtained from core samples. The magnitude of the vertical stress was calculated using the overburden weight. Since the directly measured values of the two principal horizontal stresses were not available, these stresses were then estimated using elastic moduli, and the accuracy of the results was calibrated using data obtained from a formation integrity test (FIT) conducted in the field. An image log interpretation was used to determine the orientation of the principal horizontal stresses by specifying the orientation of drilling-induced tensile fractures. Utilizing the derived stress tensor in MohrPlotter software, we investigated the stability of the faults through Mohr diagram analysis of both the current stress state and the critical state of stress caused by the gas injection. Slip tendency, an analytical parameter was also calculated, and the results were compared with the Mohr diagrams. The maximum sustainable pore pressure was calculated for each one of the faults, as the final output of these two methods. Numerical simulations were then conducted using ABAQUS software, a finite element analysis tool that is widely used for geomechanical studies. A coupled pore fluid diffusion/stress analysis was performed to model the single-phase, fully saturated fluid flow through the porous media. In the numerical simulations, gas was injected for 5 years, and the possibility of plastic damage and fault slip was assessed.

3.2 Determining the In-Situ Stress Regime

Knowing the current state of stress is the key factor for building a comprehensive geomechanical model (Zoback
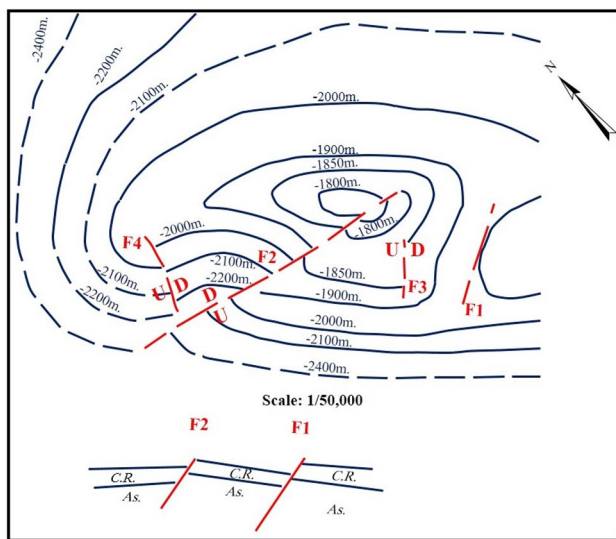
Fig. 3 Underground contour map and the cross section of the study area in the Western part of the Gachsaran oilfield

Table 1 Structural properties of faults

Fault	Dip (degree)	Dip direction (degree)	Strike (degree)	Description
F1	52	319	229	Normal fault that cuts out about 50 m of the lower part of cap rock and the upper part of Asmari formation
F2	80	8	278	Normal fault that cuts out about 20 m of the upper part of the cap rock
F3	59	130	40	Normal fault breached a small part of cap rock
F4	44	141	51	Normal fault that cuts out the cap rock completely, and 78 m of the top of Asmari formation

2007). For applying the stress concept in the Earth's crust, it is useful to consider the magnitudes of the three principal stresses (σ_1, σ_2, and σ_3) in terms of vertical (σ_V), and horizontal (σ_{Hmax} and σ_{hmin}) stresses as first proposed by Anderson (1951). In this manner, an area can be characterized as being in a normal, strike-slip, or reverse faulting stress regime. The vertical stress (σ_V) is equal to the maximum principal stress (σ_1) in a normal faulting stress regime, the intermediate principal stress (σ_2) in strike-slip stress regime, and the minimum principal stress (σ_3) in reverse faulting stress regime. The magnitude of the vertical stress can be calculated by the integration of the densities of overburden rocks as follows:

$$\sigma_V = \int_0^z \rho(z)g\mathrm{d}z \approx \bar{\rho}gz. \tag{1}$$

In this equation, $\rho(z)$ is the rock density as a function of depth, g is the gravitational acceleration constant, and $\bar{\rho}$ is mean overburden density (Jaeger and Cook 1971).

Estimating the magnitudes of horizontal stresses is a major challenge in geomechanical modeling (Zang and Stephansson 2010). A common practice for determining the magnitude of the minimum horizontal stress is to conduct a leak-off test (LOT) or an extended leak-off test (XLOT). Limited test or the formation integrity test (LT or FIT) is another field test during which the leak-off point (LOP) (the pressure required to create a hydraulic fracture) is not reached. Formation integrity tests simply indicate a maximum pressure achieved during pumping. Since this pressure is insufficient to create a fracture or growing an initiated fracture away from the wellbore, the recorded pressure does not exceed the least principal stress (Zoback et al. 2003). The FIT does not provide any information about the magnitude of the least principal stress (Konstantinovskaya et al. 2012); however, it can be used as an indicator of the lower bound of σ_{hmin}, because the pressure of a FIT will always be less than the least principal stress (Zoback et al. 2003). Only one FIT is carried out in the field and is used to calibrate the log-derived magnitudes of the minimum and maximum horizontal stresses calculated by the poroelastic horizontal strain model of Blanton and Olson (1999), as follows:

$$\sigma_{hmin} = \frac{\nu_s}{1-\nu_s}\sigma_V + \frac{1-2\nu_s}{1-\nu_s}P_P(\alpha) + \frac{E_s}{1-\nu_s^2}\varepsilon_x + \frac{\nu_s E_s}{1-\nu_s^2}\varepsilon_y, \tag{2}$$

$$\sigma_{Hmax} = \frac{\nu_s}{1-\nu_s}\sigma_V + \frac{1-2\nu_s}{1-\nu_s}P_P(\alpha) + \frac{E_s}{1-\nu_s^2}\varepsilon_y + \frac{\nu_s E_s}{1-\nu_s^2}\varepsilon_x, \tag{3}$$

where σ_V is the vertical stress, P_P is pore pressure (in MPa), α is the Biot's coefficient (which was considered 1 to account for the brittle failure of rocks), E_s is the static Young's

modulus (in GPa), and ν_s is the static Poisson's ratio. ε_x and ε_y are the magnitudes of the rock deformation in the x and y planes, which can be calculated as a function of the overburden stress as Eqs. 4 and 5:

$$\varepsilon_x = \frac{\sigma_V \times \nu_s}{E_s} \times \left(\frac{1}{1-\nu_s} - 1\right), \tag{4}$$

$$\varepsilon_y = \frac{\sigma_V \times \nu_s}{E_s} \times \left(1 - \frac{\nu_s^2}{1-\nu_s}\right). \tag{5}$$

The next step in determining the in-situ stress regime in an area is finding the orientation of horizontal stresses. Image logs provide a very useful tool for engineers to observe borehole breakouts and drilling-induced tensile fractures. The borehole breakouts and the drilling-induced tensile fractures are caused by wellbore hoop stress and radial stress, respectively (Zoback 2007). In vertical wells, the breakouts form at the azimuth of the minimum horizontal compressive stress, and drilling-induced tensile fractures
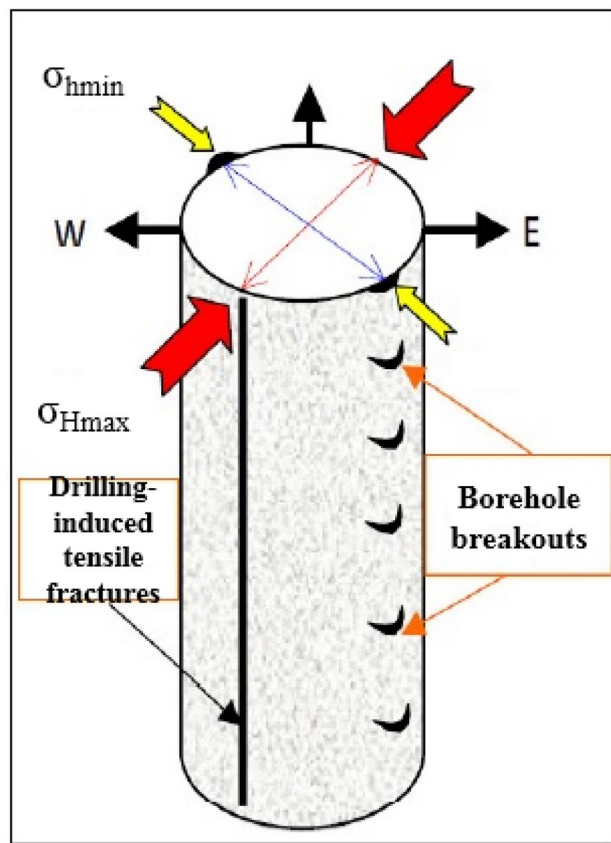

Fig. 4 Schematic illustration showing the location of the borehole breakouts and drilling-induced tensile fractures in a vertical well (Alizadeh et al. 2015). Borehole breakouts form in the direction of σ_{hmin} and drilling-induced tensile fractures form in the direction of σ_{Hmax}

form in the wall of the borehole at the azimuth of the maximum horizontal compressive stress when the circumferential stress acting around the well is locally in tension (Fig. 4).

3.3 Estimating Pore Pressure and Permeability

Direct methods of measuring pore pressure include drill stem test (DST) and repeat formation test (RFT) (Rezaee 2014). However, these methods are only utilized in a limited number of wells in the study field. Therefore, using more effective and economical methods is essential for field-wide geomechanical reservoir simulations. In this paper, the pore pressure was estimated by the modified Eaton (1975) approach derived by Azadpour et al. (2015) as follows:

$$P_{pg} = S_g - \left(S_g - P_{ng}\right)\left(\frac{50 + (185 - 50)e^{-0.00137z}}{\Delta t}\right)^x. \quad (6)$$

In this equation P_{pg} is the formation pressure gradient, P_{ng} is the hydrostatic pore pressure gradient, which equals 1.049×10^{-2} MPa/m (0.464 psi/ft) for Iran, Δt is the measured sonic transit time by well logging, z is depth, and x is the exponent constant, which was determined as 0.5 by Azadpour et al. (2015) for gas fields in southern Iran. The overburden pressure gradient S_g can be calculated by the following equation:

$$S_g = 0.433 \times \rho_b, \quad (7)$$

where the ρ_b is the bulk density. This pore pressure calculation was calibrated against repeat formation tests available from wells in this reservoir.

Permeability is one of the most important properties of a reservoir's rocks, since it controls the rate of hydrocarbon recovery. The value of this property ranges considerably from 0.01 millidarcy (mD) to over 1 darcy. A permeability of 0.1 mD is generally considered the minimum for oil production. The permeability of reservoirs with a high production rate is in the Darcy range (Lucia 2007).

The best way to measure permeability is through direct test on core samples. In this study, a few core samples were only used for destructive rock mechanical tests, and determining porosity (n) and hydraulic conductivity (k). Instead of using porosity–permeability relationships, we used global permeability transform to avoid the averaging nature of these cross plots. Given the lack of core samples, and that permeability cannot be derived from well logs, it was estimated using indirect methods. It is common practice to estimate permeability using porosity–permeability transforms developed from core data. However, porosity–permeability cross plots for carbonate reservoirs too often average out the robust permeability variations that are characteristic of carbonate reservoirs. According to Lucia (2007), the more accurate method is to use the global permeability transform

using petrophysical class or rock fabric number (rfn) and interparticle porosity (the pores that are connected). Rock fabric number is related to interparticle porosity and geologic descriptions of particle size and sorting called rock fabrics. rfn ranges from 0.5 to 4 and is defined by class-average and class-boundary porosity–permeability transforms (Jennings and Lucia 2001). The value of the rock fabric number depends on porosity and water saturation, as higher water saturation for a given porosity gives higher rfn, and lower permeability for a given porosity yields higher rfn (Crain 2017). This is a new method, designed especially for estimating the permeability in carbonates with different shapes of pores. In this approach the permeability can be calculated as follows:

$$\log(K) = (a - b\log(\text{rfn})) + (c - d\log(\text{rfn}))\log(\phi_{ip}). \quad (8)$$

In this equation, K is permeability (mD), rfn is the rock fabric number, Φ_{ip} is interparticle porosity, and a, b, c, and d are constant values ($a = 9.7982$, $b = 12.0838$, $c = 8.6711$, $d = 8.2965$). In this study, we used effective porosity log (PHIE) as Φ_{ip}. Rock fabric number can be calculated from spectral gamma ray and porosity logs using the following equation:

$$\log(\text{rfn}) = \left[A + B\log(\phi) + \lg\left(S_{wi}\right)\right]/\left[C + D\log(\phi)\right], \quad (9)$$

where rfn is the rock-fabric number ranging from 0.5 to 4 (petrophysical class may also be used), S_{wi} is the initial water saturation above the transition zone (The zone between water production and oil production), Φ is porosity, and A, B, C, and D are constants ($A = 3.1107$, $B = 1.8834$, $C = 3.0634$, and $D = 1.4045$). In this equation, total porosity log (PHIT) is used as Φ. S_{wi} is the saturation of an undisturbed reservoir with no prior production from any earlier well (Crain 2017). This parameter was available from an exploration well in the field.

The main advantage of this method is that the interparticle porosity (and not total porosity) is related to permeability (Lucia 2007).

3.4 Mechanical Properties

Evaluating the in-situ mechanical behavior of rocks requires appropriate input data such as stress state and pore pressure at the desired depth, elastic moduli, and mechanical parameters. The main data for this study come from core samples and the data recorded in the field (such as well logs, seismic data, and various well tests). In this research, we used the relationships derived by the NISOC for converting the dynamic Young's modulus (E_d) and Poisson's ratio (ν_d) to their static equivalents (E_s and ν_s), and calculating

uniaxial compressive strength (UCS) and tensile strength (σ_t), as follows:

$$E_s = 0.7 \times E_d, \tag{10}$$

$$v_s = v_d, \tag{11}$$

$$\text{UCS} = 2.27E_s + 4.7, \tag{12}$$

$$\sigma_t = 0.08 \times \text{UCS} \quad \text{Limestone}, \tag{13}$$

$$\sigma_t = 0.11 \times \text{UCS} \quad \text{Anhydrite},$$

$$\sigma_t = 0.1 \times \text{UCS} \quad \text{Shale}.$$

The above parameters were obtained by testing core samples drilled out from the reservoir and establishing statistical correlations between them. Cohesion (c) and friction angle (φ) are two mechanical properties that describe the intrinsic properties of rocks. These parameters may be determined by performing a triaxial test on the core specimens. Moreover, there are empirical and theoretical relationships that can be used when there is no access to the triaxial test. For predicting the friction angle and cohesion, Plumb's (1994) and Jaeger et al. (2009) equations were used, respectively:

$$\varphi = 26.5 - 37.4(1 - \text{NPHI} - V_{sh}) + 62.1(1 - \text{NPHI} - V_{sh})^2, \tag{14}$$

$$c = \frac{\text{UCS}}{2\tan\theta}, \tag{15}$$

where NPHI is neutron porosity, and V_{sh} is shale volume. V_{sh} and θ can be calculated using Asquith et al. (2004) and Jaeger et al. (2009) equations, respectively:

$$V_{sh} = \frac{(\text{GR}_{log} - \text{GR}_{min})}{(\text{GR}_{max} - \text{GR}_{min})}, \tag{16}$$

$$\theta = 45 + \frac{\varphi}{2}, \tag{17}$$

where GR is gamma ray. Equation 14 is a porosity based equation that predicts φ to decrease with increasing porosity and GR. Since GR is a measure of the amount of shale volume contained in a formation, this equation indicates that a rock with higher shale content has a lower internal friction angle (Chang et al. 2006). The cohesion equation (Eq. 15) is derived from UCS relationship in direct shear tests. In this equation, cohesion is a function of UCS and θ, which the latter one depends on the friction angle.

3.5 Analytical Methods of Fault Stability Evaluation

The possibility of fault reactivation to provide a flow path in faulted areas first was introduced by Sibson (1990), and the process is generally controlled by the Coulomb failure criterion. The three main approaches for evaluating this phenomenon are: analytical, semi-analytical, and numerical (Nacht et al. 2010). Mohr diagrams, slip tendency, and dilation tendency are some of the most common and widely used analytical methods.

One of the best ways to show the shear and normal stresses acting on arbitrarily oriented faults in three dimensions is the Mohr diagram (Zoback 2007). These diagrams are also applied to explain the mechanism of faulting and reactivation of pre-existing faults (Yin and Ranalli 1992; Jolly and Sanderson 1997; McKeagney et al. 2004; Streit and Hillis 2004; Xu et al. 2010).

The values of the three principal stresses σ_1, σ_2, and σ_3 are used to construct three Mohr circles. The largest Mohr circle is defined by the difference between σ_1 and σ_3, and the two smaller Mohr circles are defined by the differences between σ_1 and σ_2, and σ_2 and σ_3, respectively (Zoback 2007). Fault planes are represented in Mohr diagrams by their normal stress, σ_n, and shear stress, τ. These stresses are shown in Fig. 5 and can be readily calculated using the following equations:

$$\sigma_n = \sigma_V(\cos\beta_1)^2 + \sigma_H(\cos\beta_2)^2 + \sigma_h(\cos\beta_3)^2, \tag{18}$$

$$\tau = \sqrt{\sigma_V^2(\cos\beta_1)^2 + \sigma_H^2(\cos\beta_2)^2 + \sigma_h^2(\cos\beta_3)^2 - \sigma_n^2}. \tag{19}$$

As shown in Fig. 5, β_1, β_2, and β_3 are the angles between the surface normal (n) and the axes of the greatest, intermediate, and least principal stresses, respectively. In this study, the open-source MohrPlotter software was used to calculate these angles and the stresses on the fault planes.

To estimate the maximum sustainable pore pressure on a fault, the fluid pressure increase required to induce failure on faults must be calculated. In a Mohr diagram, this pore pressure increase is the difference between the effective normal stress acting on a fault segment and the effective normal stress required to cause failure in this segment (Streit and Hillis 2004). For the case of a fault plane with cohesion (i.e., $c \neq 0$), the critical pore pressure is measured as the difference between the initial and final states when the Mohr circle reaches the Griffith-Coulomb failure envelope. However, in most cases, the cohesion of the faults is assumed to be zero (i.e., $c = 0$); therefore, the Coulomb failure envelope is applied (Fig. 6).
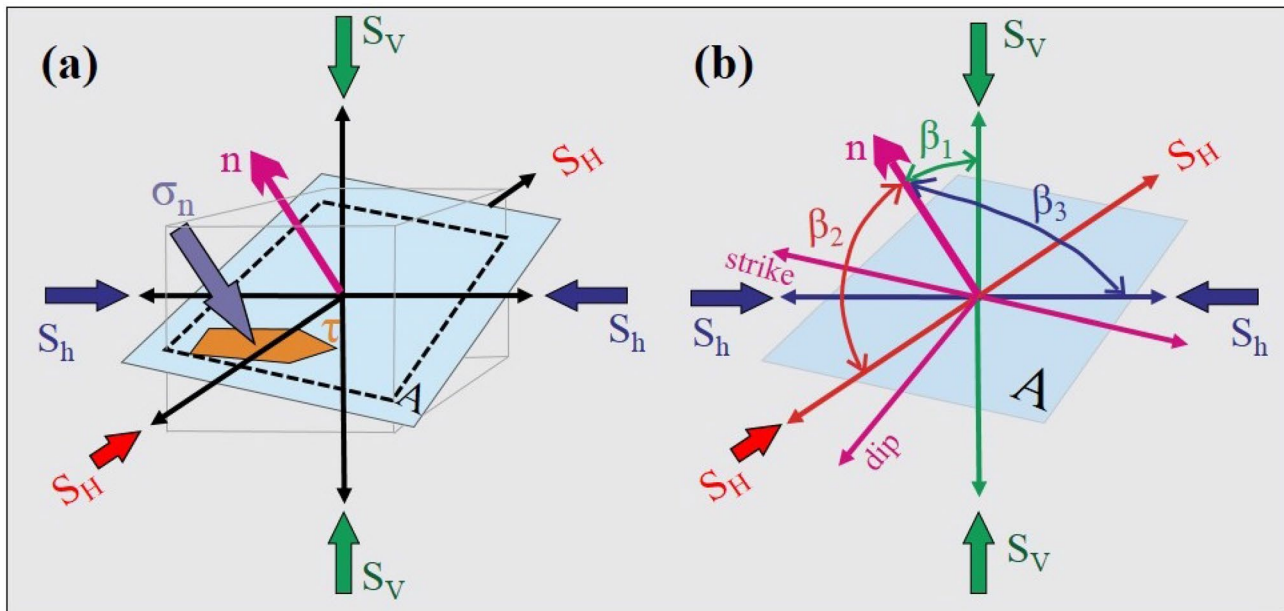
Fig. 5 **a** Resolved normal (σ_n) and shear (τ) stress on plane A. **b** Orientation of the potential slip plane A in terms of three angles $\beta1$, $\beta2$, and $\beta3$ from the coordinate axes of the principal stresses (Schmitt 2014)
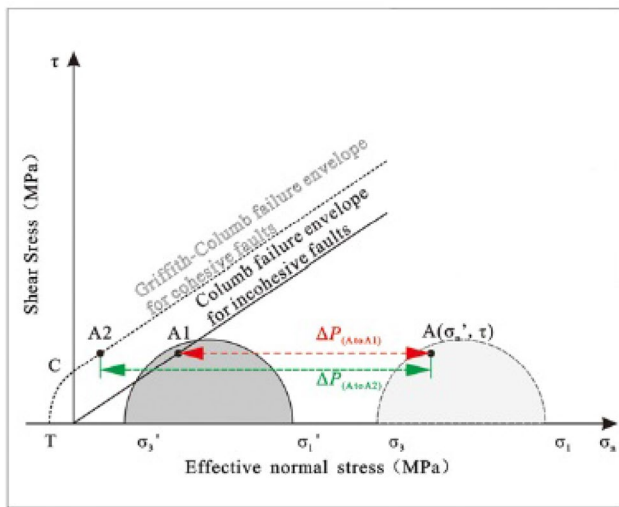

Fig. 6 Maximum sustainable pore pressure for two states of faults with and without cohesion. ΔP_{A-A1} and ΔP_{A-A2} represent the maximum sustainable fluid pressures of incohesive and cohesive faults, respectively (Meng et al. 2016)

Simply reaching the failure envelope does not mean that the failure will occur, and the planes of weakness must lie within a range of specific orientations. To find these sets of orientations, failure envelopes for both intact rock ($c \neq 0$) and pre-existing fractures ($c = 0$) must be defined (Fig. 6). In the rectangular core sample shown in Fig. 7, only the possible planes of weakness with orientations within the

pink region will be reactivated; therefore, the reactivation angle (the angle between the σ_1 axis and the fault plane) should be calculated.

To better explain the possible reactivation angles, we consider a Mohr diagram (Fig. 8), in which the red lines represent failure envelopes for a specific plane in the rock (e.g., pre-existing faults). In this case, some portions of the Mohr circle are above the failure envelope, because the orientation of the plane relative to the principal stresses is critical (critically stressed and favorably oriented faults). Consider, for example, the plane represented by the green line in Fig. 8. The associated shear and normal stress tractions associated with this plane (on the circle) are well below the failure envelope and so it is stable. If the plane was instead oriented in the range between the two orange lines (labeled as the unstable range) the shear stress would be above the failure envelope and slip should have occurred (Muvdi and McNabb 1991). In reactivation angle analysis we try to identify the unstable ranges as angles with respect to principal stresses orientations.

Fault slip occurs when the maximum shear stress acting on the fault plane exceeds the shear strength of the fault plane. Slip tendency is a method that allows quick assessment of stress states and related potential fault activity (Morris et al. 1996). Using two-dimensional stress equations given by Jaeger and Cook (1969), the values of shear and normal stresses on the fault plane can be calculated as follows:
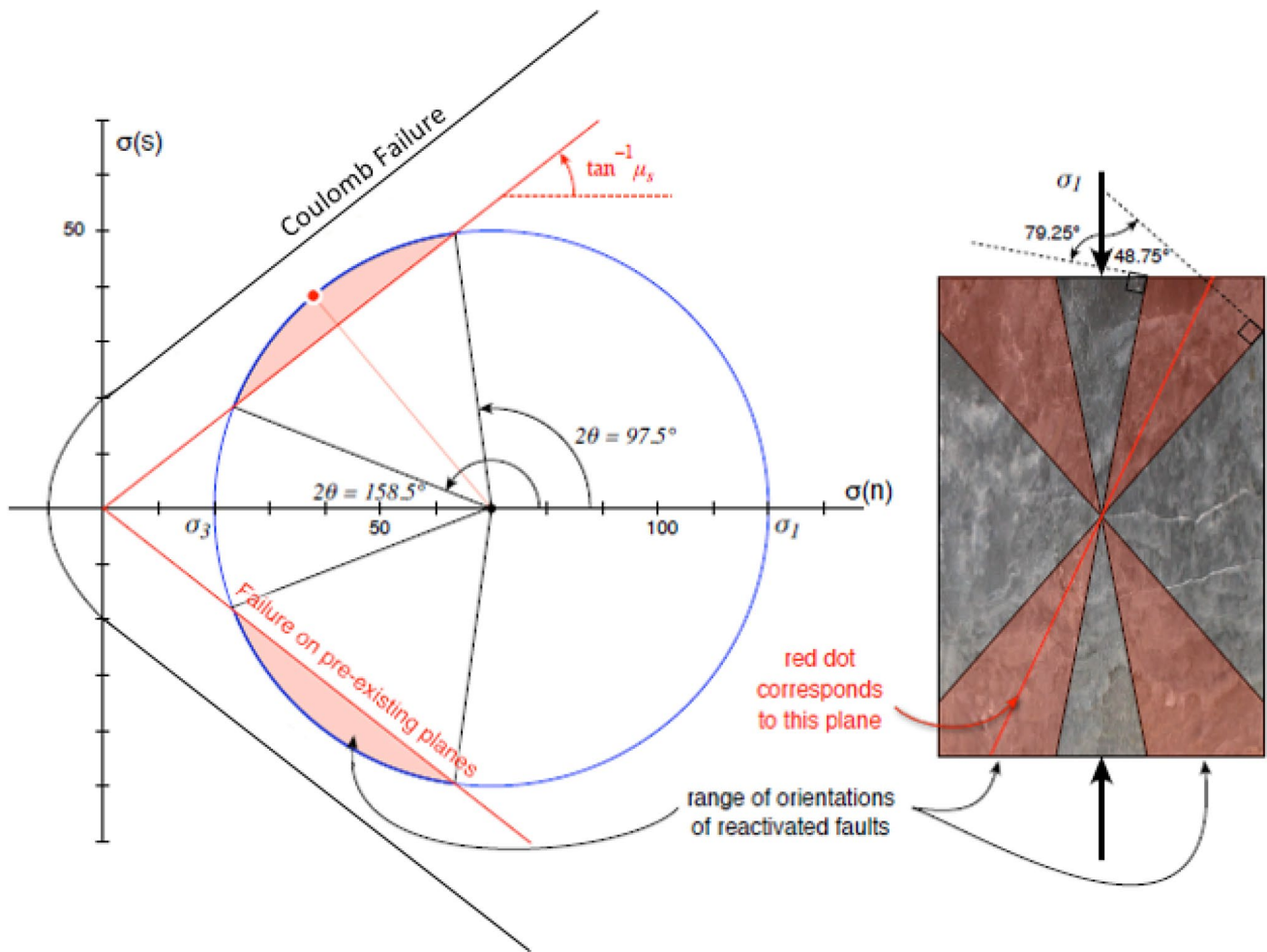
Fig. 7 Mohr diagram plotted for pre-existing fractures (red envelope), and new fractures (black envelope). Planes which their normal and shear stresses fall within the pink region will be reactivated (Allmendinger 2017) (color figure online)
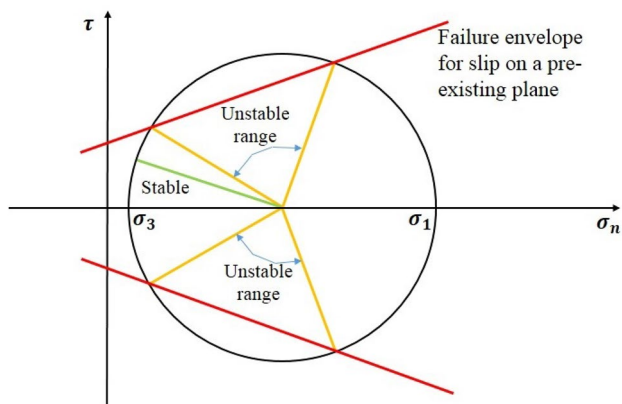
Fig. 8 Mohr circle showing the concept of reactivation angles as stable and unstable ranges for critically stressed and favorably oriented faults

$$\sigma_n = \frac{(\sigma_1 + \sigma_3)}{2} - \frac{(\sigma_1 - \sigma_3)}{2} \cos 2\theta, \tag{20}$$

$$\tau = \frac{(\sigma_1 - \sigma_3)}{2} \sin 2\theta, \tag{21}$$

where θ is the angle between the normal to the fracture plane of and σ_1.

The ratio of shear to normal stress acting on the surface is the slip tendency (T_S) and is defined as:

$$T_s = \tau/\sigma'_n. \tag{22}$$

In this equation, τ is the shear stress, and σ'_n is the effective normal stress ($\sigma_n - P_P$). According to Rutqvist et al. (2007), for a cohesionless fault, the slip will occur when the following condition is met:

$$\tau/\sigma_n' \geq \mu_s, \tag{23}$$

where μ_s is the static frictional coefficient.

In Mohr diagrams, the critical pore pressure is the pore pressure at which the effective normal stress decreases such that the point representing the fault plane reaches the failure envelope (Fig. 6). According to Eq. 23, the potential for fault slip can be expressed in terms of the fluid pressure required to induce slip. The critical pore pressure (P_C), can be calculated from effective stress law of Terzaghi (1923) (Eq. 24) and Coulomb failure criterion (Jaeger et al. 2009) (Eq. 25), as follows (Eq. 26):

$$\sigma_n' = \sigma_n - P_P, \tag{24}$$

$$\tau = c + \mu_s \sigma_n', \tag{25}$$

$$P_C = \sigma_n - \frac{\tau}{\mu_s}, \tag{26}$$

where P_P is pore pressure. By considering the Coulomb constitutive model for the fault, the shear slip potential can be expressed in terms of effective principal stresses as follows:

$$\sigma_1' = c + q\sigma_3', \tag{27}$$

where c is cohesion, σ_1' is the maximum effective principal stress, σ_3' is the minimum effective principal stress, and q is the slope of the line σ_1' versus σ_3', which is related to μ_s according to the following equation:

$$q = \left[\left(\mu_s^2 + 1 \right)^{\frac{1}{2}} + \mu_s \right]^2. \tag{28}$$

By substituting a zero cohesion into Eq. 27 and a static coefficient of friction of 0.6 into Eq. 28, the following equation is obtained (Rutqvist et al. 2007):

$$\sigma_1' = 3\sigma_3'. \tag{29}$$

Equation 29 indicates that the shear slip will be induced whenever the maximum principal effective stress exceeds three times the minimum compressive effective stress. Therefore, the critical pore pressure (P_C) required to induce slip on an arbitrarily oriented fault can be calculated as follows (Rutqvist et al. 2007; Figueiredo et al. 2015):

$$P_C = \frac{3\sigma_3 - \sigma_1}{2}. \tag{30}$$

Taghipour et al. (2019) demonstrated that this simple 2D analysis could estimate the critical pore pressure with acceptable accuracy, and its results were consistent with the results of Mohr diagrams. Therefore, this method can be used as a substitute when there is no access to image logs for constructing a Mohr diagram.

Dilation tendency analysis, first introduced by Ferrill et al. (1999), investigates the ability of a fault to act as a fluid conduit by reactivation in the current stress field or intact rock to undergo tensile failure into the cap rock (hydraulic fracturing) (Kulikowski et al. 2016). In other words, this parameter highlights the faults or fault segments within a reservoir that are critically stressed, and therefore, likely to transmit fluids (Siler et al. 2016; Ferrill et al. 2019). This analysis is most useful in reservoirs that are fault sealing or have faults that cut both the reservoir and overlying cap rock, since it predicts the chance of tertiary migration of hydrocarbons through a permeable conduit away from the reservoir (Barton et al, 1995; Ferrill and Morris 2003; Jolie et al. 2015). The dilation of faults and fractures is mainly controlled by the resolved normal stress, which is a function of the lithostatic and tectonic stresses, and fluid pressure. Based on Eq. 18, the magnitude of normal stress can be computed for surfaces of all orientations within a known or suspected stress field. The normal stress can be normalized by the differential stress to give the dilation tendency (Moeck et al. 2009). Dilation tendency is calculated using the following equation:

$$T_d = \frac{\sigma_1' - \sigma_n'}{\sigma_1' - \sigma_3'}, \tag{31}$$

where T_d is dilation tendency, σ_1' is the maximum effective principal stress, σ_3' is the minimum effective principal stress, and σ_n' is the effective normal stress acting on the fault plane. This relationship shows that as σ_n' approaches σ_3', the tendency of the fault plane to dilate increases and remains open to potential fluid flow. The fault will have a higher dilation tendency as T_d approaches one. Dilation and fluid transmission ability of a fault or fracture is directly related to its aperture, which in turn is a function of the normal stress acting upon it. Faults or fractures with high normal stress are more likely to be closed than those with lower normal stress acting to close them (Ferrill et al. 2019). As a result, permeability perpendicular to the minimum principal stress direction (i.e., the σ_1–σ_2 plane) is relatively enhanced, because lower resolved normal stress results in less fracture aperture reduction (e.g., Carlsson and Olsson 1979). Dilation tendency is strongly controlled by resolved normal stress and can highlight which fracture orientations are most likely to dilate and hence transmit fluids. Higher dilation tendency values equate to a greater likelihood of fracturing causing dilation and hence a greater ability to allow fluid transmission (Grosser 2012). In general, the planes perpendicular to the minimum principal stress show the highest dilation tendency in a given stress field (Jolie et al. 2015). A
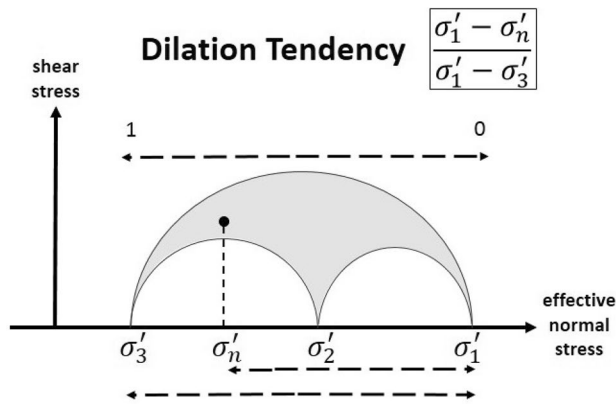
Fig. 9 Definition of dilation tendency (Mildren et al. 2005). T_d values range from 1, a fault plane that is ideally oriented to slip or dilate under current stress field to zero, a fault plane with no potential to slip or dilate

schematic illustration of the dilation tendency in the Mohr diagram is shown in Fig. 9.

3.6 Numerical Approach of Fault Stability Evaluation

Although analytical methods are acceptable for a preliminary evaluation of fault stability, some of the simplifications characteristic of these methods cannot adequately represent the specifications of the reservoir. As observed in depleted reservoirs and validated by numerical modeling, the in-situ stress field does not remain constant during injection, but rather evolves in time and space, controlled by the evolutions of fluid pressure and temperature, and site-specific reservoir geometry (Hillis 2001; Rutqvist and Tsang 2005; Hawkes et al. 2005; Rutqvist et al. 2007).

In this study, numerical simulations were carried out using ABAQUS software, a finite element analysis code, which is widely used for geomechanical studies. The solver used in this study is Abaqus/Standard that is quite suitable for a wide range of geomechanical problems with coupled pore fluid-stress analysis. The main goals of these

simulations include: (1) investigating the fluid flow in the reservoir-cap rock system, (2) the possibility of gas leakage through the cap rock, (3) possible fault reactivation, and (4) the propagation of shear stress and plastic strain in various parts of the reservoir.

The geometry of this 2D model is rectangular with dimensions of 7000 m length and 600 m width, which represents the layers of Gachsaran cap rock, Asmari reservoir, Pabdeh source rock, and the four faults F1–F4 within the depth range of 2000–2600 m (Fig. 10). The thickness of the reservoir was considered constant (nearly 300 m). To simulate fault throw (i.e., the amount of vertical displacement of rocks), the thickness of the cap rock was considered variable (50–200 m). The magnitude of the fault throw for each fault was measured in faulted wells in the field. An equivalent overburden is included in the model to the reservoir depth of 2000 m. The hydraulic boundary conditions of the model include a constant hydrostatic pressure at the outer boundary and no flow at the other boundaries. For the mechanical boundary conditions, a constant overburden pressure is applied on the upper boundary and displacement perpendicular to the other boundaries is fixed. The model mesh consists of quadratic pore fluid-stress elements with reduced integration (CPE8RP). A friction coefficient of $\mu = 0.6$ is assumed for the faults, and the faults are simulated as fault zones (with a fault core in the middle of two adjacent damage zones). To simulate injection, constant pore pressure of 30 MPa was applied for 5 years through a vertical well located in the westernmost part of the model. The distance between the injection point and the nearest fault (F4) is about 560 m. The Coulomb failure criterion is used to indicate the onset of fault shear slip. The calculated horizontal/vertical stress ratios of 0.74 in the x–y plane, and 0.85 normal to this plane were considered. The hydraulic and mechanical properties of different parts of the model are summarized in Table 2. In this table E_s, ν_s, c, φ and σ_t were calculated using Eqs. 10–15, and k and n were obtained from laboratory tests carried on core samples by the NISOC. Note that the c values for fault core and damage zone in this table are related to the rocks of these
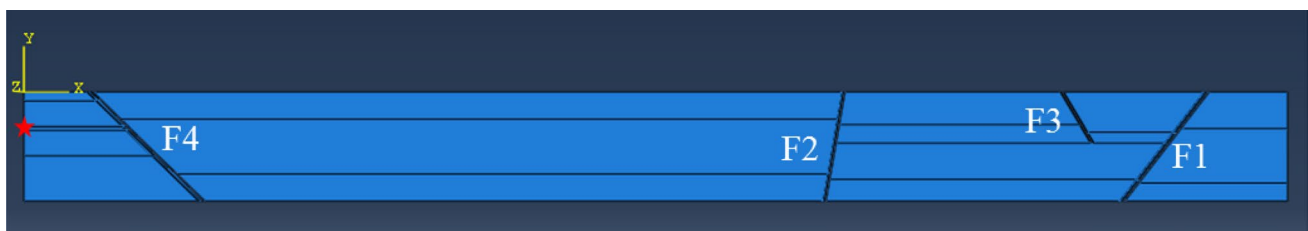
Fig. 10 Schematic illustration of the 2D model (the red asterisk shows the location of the injection point) (color figure online)

Table 2 Hydraulic and mechanical properties of the model

Property	Cap rock	Reservoir	Basement	Fault core	Damage zone
φ (°)	36	31	27	36	31
c (MPa)	21.1	20.9	19.0	21.1	20.9
E_s (GPa)	25	38	25	25	38
ν_s	0.30	0.28	0.30	0.30	0.28
σ_t (MPa)	5.5	8.3	6.5	6.5	8.3
k (m/s)	1.0×10^{-12}	7.3×10^{-8}	1.8×10^{-10}	1.0×10^{-12}	2.2×10^{-7}
n (%)	0.9	10	4.7	0.9	10

regions and not to the fault surface, where its cohesion is considered zero.

No information was available to characterize the properties of the fault core and damage zone; therefore, their properties are mainly considered to be the same as the cap rock and reservoir, respectively. Due to the highly fractured nature of the rocks caused by shearing in the damage zone, the permeability of this zone is assumed to be an order of magnitude greater than the reservoir (Jeanne et al. 2014; Yoon et al. 2016).

4 Results and Discussion

4.1 Stress Magnitudes and Mechanical Properties

To investigate the stability of the faults in this reservoir, the current stress field was estimated using density logs and poroelastic equations, as described above. For this reservoir, the vertical stress (σ_V) is the maximum principal stress (σ_1), and the intermediate and minimum principal stresses (σ_2 and σ_3), are σ_{Hmax} and σ_{hmin}, respectively, and thereby classified as a normal faulting regime (i.e., $\sigma_1 > \sigma_2 > \sigma_3$) (Anderson 1951). Figure 11 shows the stress profile for the field. In this figure, σ_V, σ_H, σ_h and P_p are shown with the line of best fit (smooth scatter lines and points of these parameters are hidden). In this figure, the estimated P_p (red line) and directly measured P_p at 17 points within the reservoir (gray points) show a maximum difference of 2 MPa, which is consistent with an acceptable range for the accuracy when applying the Azadpour et al. (2015) method. In this field, the hydrostatic pressure (blue dashed line) is higher than the estimated pore pressure (red dotted line) (Fig. 11), which means that the field is under-pressured and confirms the necessity of gas injection. The interpreted image log showing the drilling-induced tensile fractures is illustrated in Fig. 12. In addition to interpreting the image log for the orientations of horizontal stresses, the population of natural fractures was measured. A total number of 32 fractures with
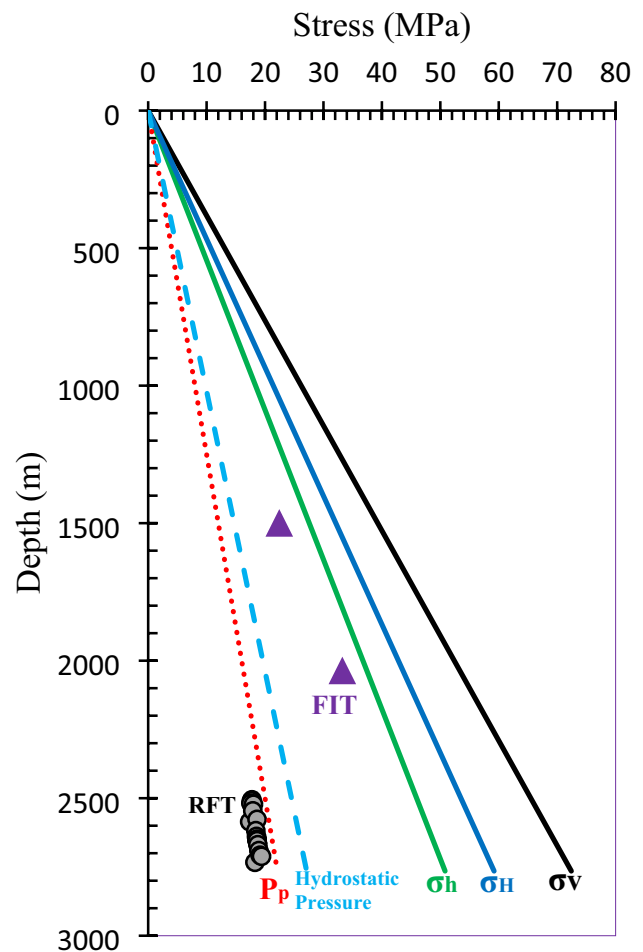

Fig. 11 Stress-depth plot showing the stress state in Gachsaran oilfield (the principal stresses and pore pressure are plotted with the line of best fit). The gray points represent the formation fluid pressures (RFT), and triangles indicate FIT pressure (the stresses are calculated using the elastic moduli estimated by NISOC equation)

a dominant azimuth of 52° were observed. Based on the fact that the existence of drilling-induced tensile fractures is 90° from borehole breakouts (Fig. 4), the azimuths of the two principal horizontal stresses were determined 52° for σ_{Hmax} and 142° for σ_{hmin}. Figure 13 shows the fault planes and in-situ stresses orientations in lower hemisphere stereographic projection.

The mechanical properties of the rocks were estimated using Eqs. 10–17. Figure 14 shows these properties along a well. These properties were calculated for all the wells and were used for constructing Mohr diagrams and numerical models.

4.2 Analytical Methods

Mohr diagrams were constructed for the four faults, and the maximum sustainable pore pressure calculated for each.
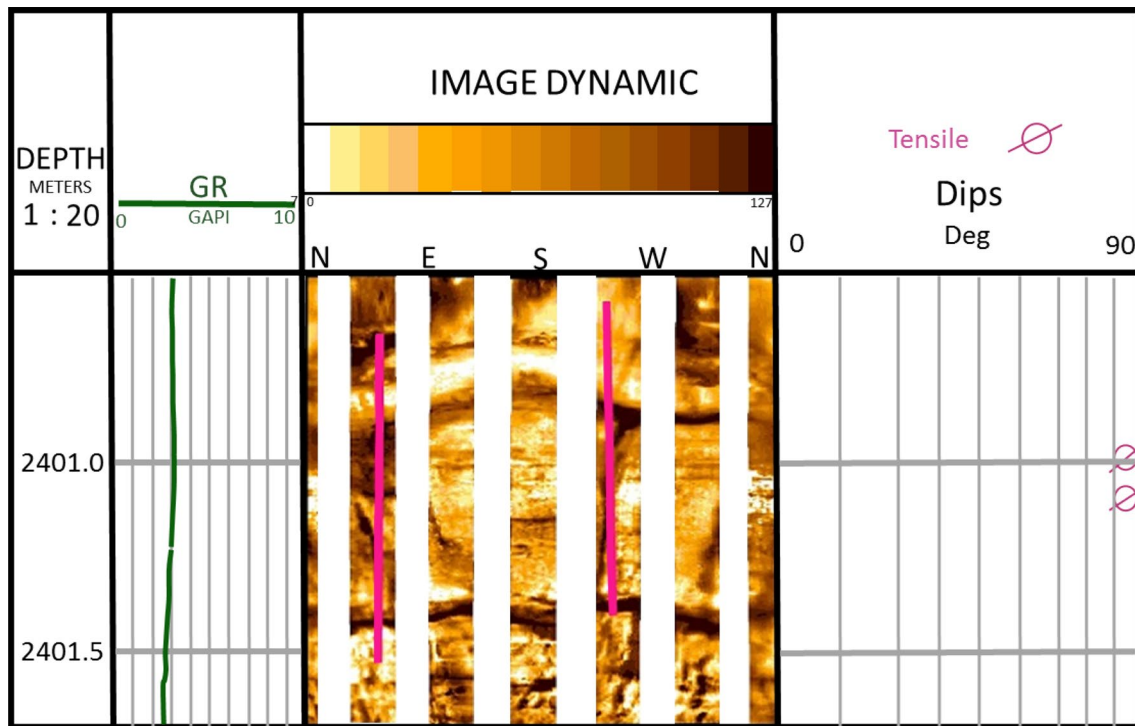
Fig. 12 Interpreted image log showing the locations of the drilling-induced tensile fractures (pink lines). These fractures show a dominant azimuth of 52° that corresponds to the direction of σ_{Hmax} (color figure online)
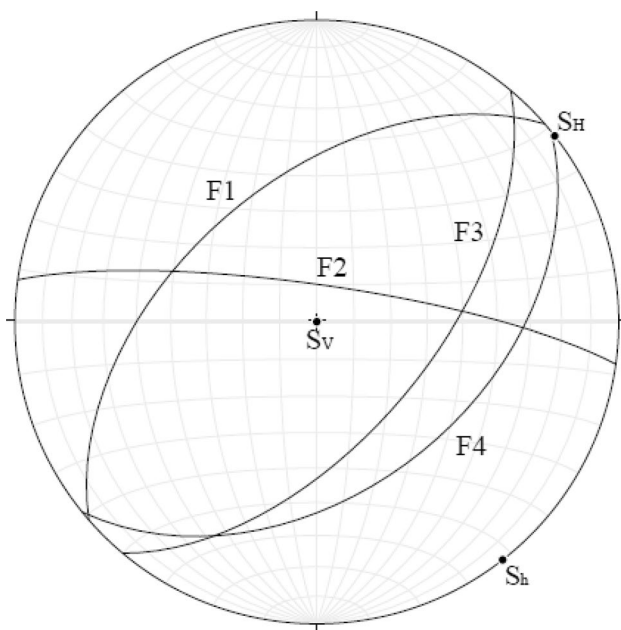

Fig. 13 Stereographic projection of fault planes and in-situ stresses orientations. The azimuths of σ_{Hmax} (S_H) and σ_{hmin} (S_h) are 52° and 142°, respectively

Figure 15 shows the Mohr diagram plotted for F1 in the current stress conditions and Fig. 16 shows the Mohr diagram for the same fault at the pore pressure required to induce shear slip. The results of this analysis for all the faults are summarized in Table 3.

The results show that in the current stress field and pore pressure, all the faults are stable and lie below the failure envelope. In Table 3, σ'_{ni} and τ represent the current effective normal and shear stress acting on the faults. P_{pi} is the current pore pressure estimated for the field. P_{pmax} is the maximum sustainable pore pressure, calculated by increasing the pore pressure such that the Mohr circle reaches the failure envelope. ΔP_p is the difference between P_{pi} and P_{pmax}, and σ'_{nf} is the effective normal stress after increasing the pore pressure. The highest P_{pmax} was calculated for F2 (57 MPa), indicating this fault has the highest stability against injection.

For investigating the propagation of new fractures induced by injection (hydraulic fracturing), the Mohr failure envelope was constructed for intact rocks. The tensile strength and cohesion of the reservoir and cap rock were estimated using Eqs. 13 and 15, respectively. Figure 17 shows the injection pressure required to induce new fractures (intact rock) for the stress magnitudes in the vicinity of F1 (i.e., the pressure at which the effective normal stress
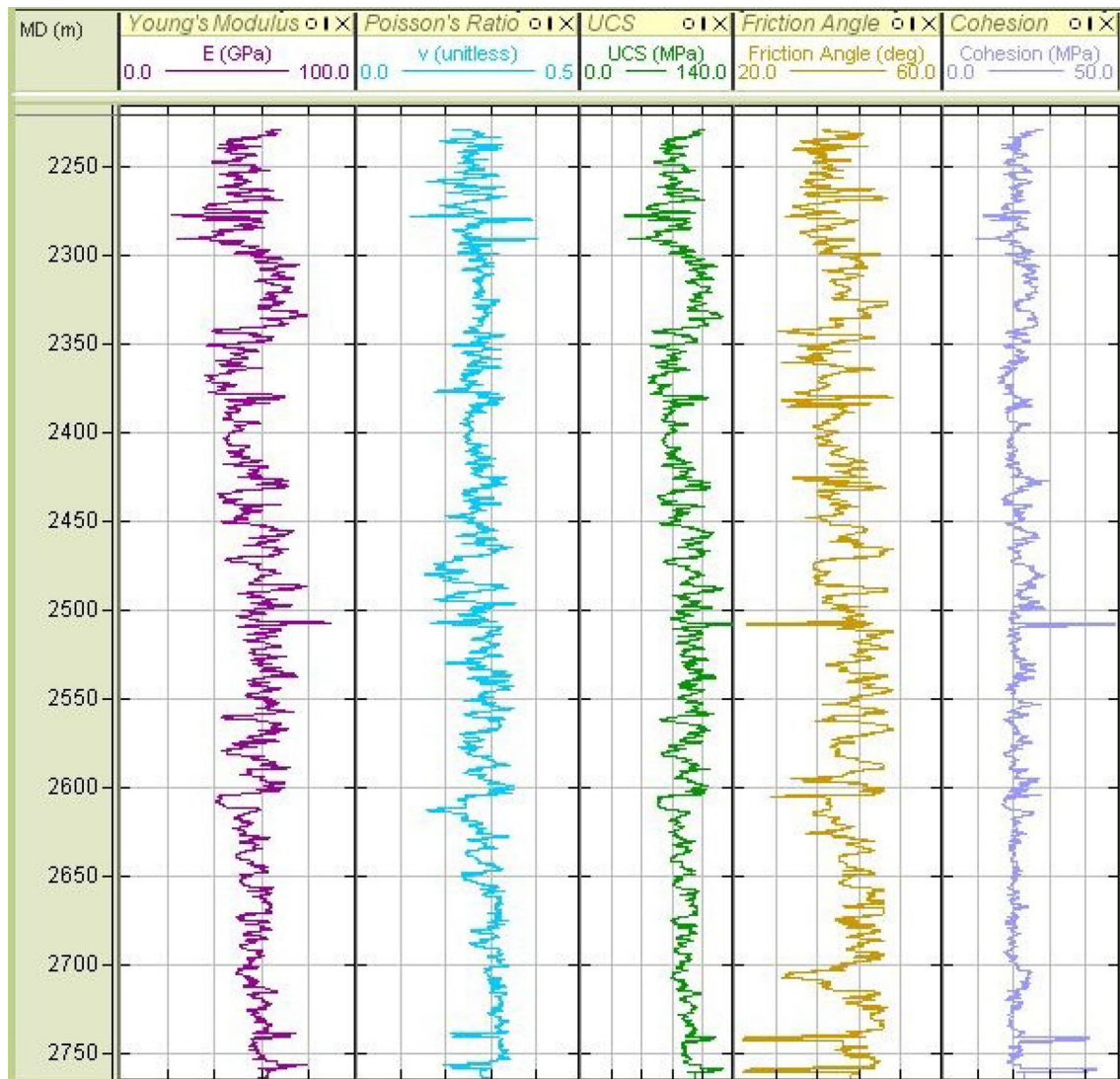
Fig. 14 Logs of static Young's modulus, Poisson's ratio, uniaxial compressive strength (UCS), friction angle and cohesion in a well. These properties are crucial for numerical modeling

is < 0). The remaining results for this analysis are summarized in Table 4.

The results suggest that for the stress magnitudes around F1, intact rock in the reservoir will undergo tensile fracturing at an injection pressure around 59 MPa. It was also found that the pressure needed to create a fracture around F1 and F3 is less than F2 and F4, which divides the area into two regions, one with a lower strength (west to southwest) and the other higher strength (northwest). Using open-source MohrPlotter software, the potential angles for reactivation of these fractures were calculated (Table 5).

In Table 5, the reactivation angles calculated for F3 and F4 are nearly similar. The reason is that as shown in Fig. 13, these faults have similar strikes and orientations to

the principal stresses, which means F3 and F4 are nearly two similar planes subjected to the in-situ stresses.

The slip tendency (T_s), the critical pore pressure (P_C), and dilation tendency (T_d) were calculated using Eqs. 22, 30, and 31. As shown in Table 6, again all the faults are stable in the current stress field, since their slip tendency is lower than the assumed frictional coefficient ($\mu = 0.6$).

In a normal fault stress regime, the faults that are most likely to slip tend to have a strike sub-parallel to the intermediate in-situ principal stress ($\sigma_2 = \sigma_{Hmax}$) and dip at roughly 60 degrees (Hawkes et al. 2005). In the study area, F1, F3, and F4 have strikes nearly parallel to the σ_{Hmax} orientation, but only the dip of F3 is 59° (Table 1). Based on the results of both Mohr diagrams (Table 3) and slip tendency equation (Eq. 22 and Table 6), F3 is more likely
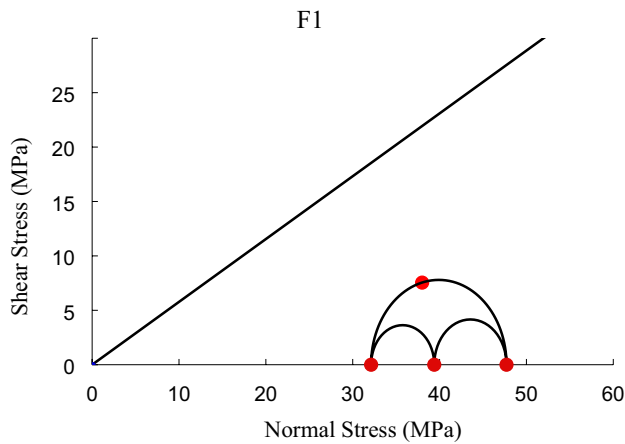
Fig. 15 Mohr diagram for the cohesionless F1 in the current stress field. As shown, this fault is stable in the current stress field (before injection). The red dot on the big circle (σ'_1–σ'_3) shows the shear and normal stresses for this fault
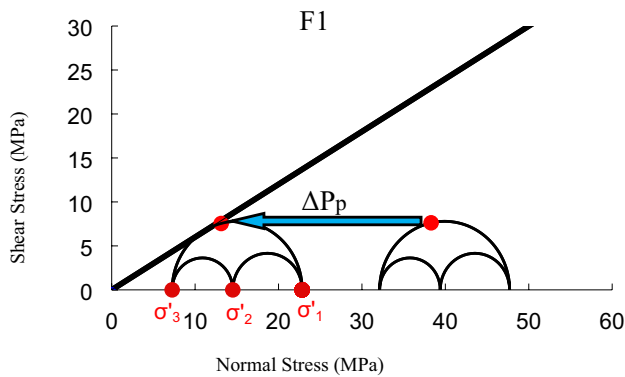
Fig. 16 Mohr diagram plotted for F1 for estimating critically stressed pore pressure. The pore pressure increase to cause failure (ΔP_p) for this fault is about 24.9 MPa

to reactivate than the other faults, since its ΔP_p and P_{pmax} are lower. F3 also has the highest slip tendency value, which means it can reactivate with a lower pore pressure increase. On the other hand, F2 is the most stable fault based on both methods of Mohr diagrams and slip tendency parameter, with the lowest T_s and average maximum

pore pressure of 55–57 MPa. The highest dilation tendency is computed for F3, which is perpendicular to the minimum horizontal stress. This means that this fault has a high potential to remain open against fluid flow. Since T_d also provides the potential for tensile failure, this potential is high for F3, because it will undergo tensile fracturing at lower injection pressures.

4.3 Numerical Modeling

The first step of the analysis is a geostatic step to equilibrate geostatic loading of the model. This step also establishes the initial distribution of pore pressure. Results of this step confirm that displacements are very small and the model is in geostatic equilibrium (Fig. 18). In this figure, the maximum magnitude of displacements (the resultant displacement of *x* and *y* directions) around F4 is 0.09 μm.

The numerical simulation of gas injection into the reservoir was carried out, starting with a 30 MPa pressure for 5 years. The volume of the injected gas for this injection pressure and period is about 581.5 m³ (Fig. 19).

Simulation results using F4 geometry indicate that the injected gas plume moves both forward and upward over time. The ascending gasses are the main reason for hydraulic fracturing in the cap rock and can generate cap rock integrity issues. After two hours, the gas plume has traveled about 150 m away from the injection point in the reservoir (Fig. 20). Results show that the damage zone of the fault acts as a conduit because of its higher permeability than the fault core. Through this conduit, the pore pressure plume penetrates the Pabdeh source rock and the cap rock. Also, the ascending gasses from the reservoir infiltrate the lower part of the cap rock at the end of 5 years (Fig. 21). From this time forward, the gas plume will start to fully penetrate the cap rock from both the damage zone and the reservoir-cap rock interface. Generally, because the fault core is practically impermeable, gas injection in each block of the compartmentalized reservoir leads to the overpressures in that block and prevents the gas from infiltrating the other section beyond the fault (Fig. 22). And finally, this stored gas induces uplift (~ 11 cm) above the injection area (Fig. 23).

Table 3 Effective normal and shear stress, initial pore pressure (Ppi), the maximum sustainable pore pressure (Ppmax), pore pressure increase (ΔPp) and normal stress at failure point (σ'nf) for the faults

Fault	σ'_{ni} (MPa)	τ (MPa)	P_{pi} (MPa)	P_{pmax} (MPa)	ΔP_p (MPa)	σ'_{nf} (MPa)
F1	37.99	7.54	19.13	44.0	24.9	13.12
F2	42.07	3.64	22.04	57.4	35.4	6.71
F3	32.52	7.85	19.87	38.8	18.9	13.59
F4	40.61	8.54	22.07	48.0	25.9	14.69
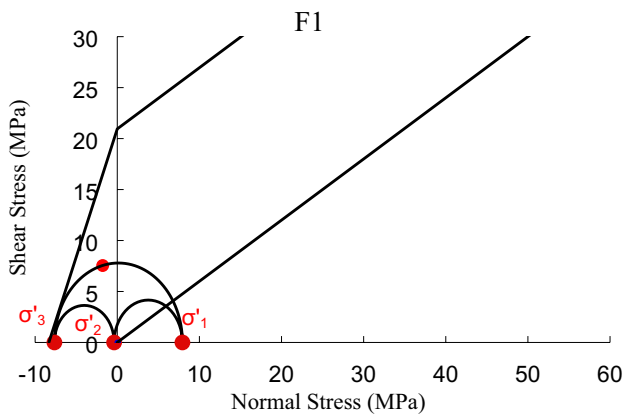
Fig. 17 Mohr diagram of F1 and intact rocks in the current stress field. For this fault, the intact rock in the reservoir will undergo tensile fracturing at an injection pressure of 59 MPa

Table 4 Pore pressure required to induce new fractures in the stress condition around each fault

Fault	P_p required to induce new fractures (MPa)	
	Cap rock	Reservoir
F1	56.3	58.9
F2	65.4	68.1
F3	52.5	55.1
F4	58.8	61.5

The pore pressure increase as a function of distance along a cross section perpendicular to F4 including the fault core and adjacent damage zone is shown in Fig. 24. As shown in this figure, the sharp decrease in pore pressure on the right side of the fault is due to the impermeable fault core that acts as a barrier and prevents the gas plume from spreading. The pressure evolution in the adjacent damage zone of F4 as a function of time is presented in Fig. 25. This figure also shows the importance of the

Table 6 Values of slip tendency (Ts), critical pore pressure (P_C), and dilation tendency (Td) for the faults

Fault	T_s	P_C (MPa)	T_d
F1	0.19	43.45	0.62
F2	0.04	55.03	0.63
F3	0.24	38.51	0.73
F4	0.21	45.34	0.48

impermeable fault core in preventing the pore pressure increase. The pore pressure on the left side of the fault (near the injection zone) reaches 30 MPa after a short time (~ 6 months), but on the right side, it shows a slight increase (~ 0.5 MPa) after 5 years. The maximum shear stress accumulated after injection is about 13 MPa on F4, and about 8 MPa on the other faults (Figs. 26, 27). This difference is because of the higher gas accumulation on the F4 surface, which is closer to the injection zone.

In this study, the plastic plane strain was monitored. This is a two-dimensional state of strain in which all the shape changes of material happen on a single plane (the x–y plane in our case), and stress along z-direction is zero. Based on the findings, no plastic strain or fracture growth was initiated by applying an injection pressure of 30 MPa (Fig. 28). Therefore, this pressure can be assumed as the safe lower bound of injection pressure for this field. This result was also confirmed by the analytical methods.

We further investigated the effect of injection pressure increase on fault stability by increasing injection pressure to 50 MPa. After approximately 100 days of injection, the plastic strains started to develop on the fault plane (Fig. 29). These strains are directly related to the development of new fractures and imply the start of fault reactivation. According to the results of the geostatic step and injection pressure of 30 MPa, the model is stable, and no deformation was observed in these steps. Therefore, the only factor that can cause deformation in 50 MPa pressure is the pore pressure increase caused by injection. Since the gas was injected into the reservoir and these strains initiated in the cap rock, they seem to be the result of fault slip. These deformations are

Table 5 Possible reactivation angles of new fractures

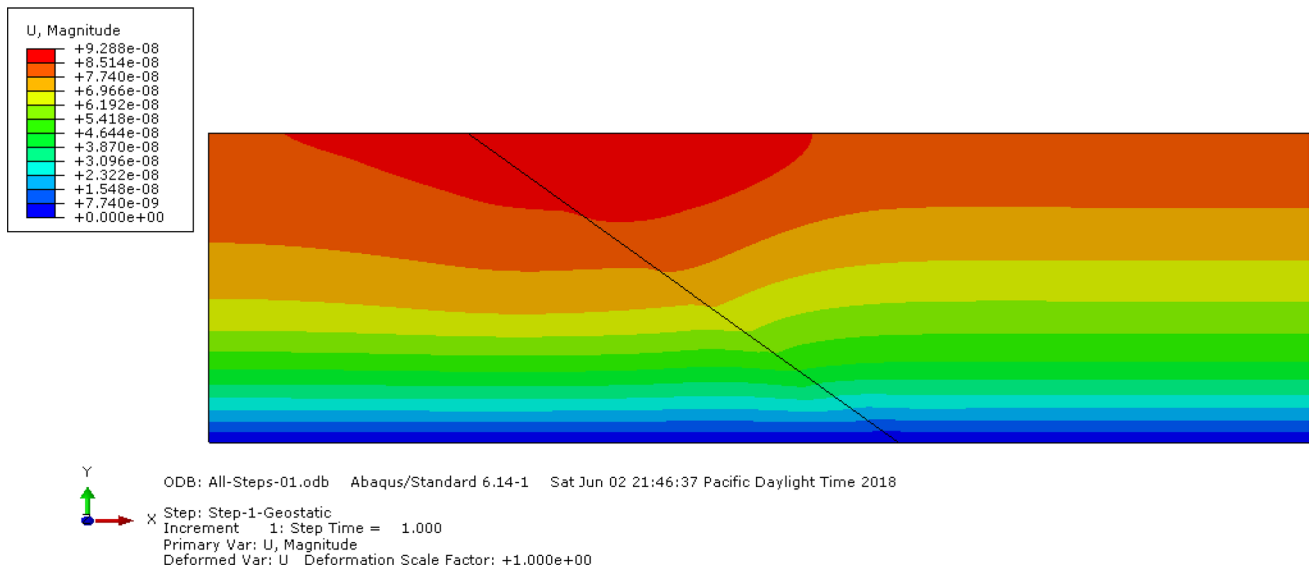| Fault	Possible reactivation angles
F1	Planes parallel to σ_2 with a pole between 19.6° and 11.2° with respect to σ_1 will be reactivated
	Planes parallel to σ_1 with a pole between 47.6° and 73.3° with respect to σ_2 will be reactivated
	Planes parallel to σ_3 with a pole between 10.3° and 20.5° with respect to σ_1 will be reactivated
F2	Planes parallel to σ_2 with a pole between 29.6° and 1.3° with respect to σ_1 will be reactivated
	Planes parallel to σ_1 with a pole between 51.3° and 69.5° with respect to σ_2 will be reactivated
	Planes parallel to σ_3 with a pole between 27.0° and 3.9° with respect to σ_1 will be reactivated
F3	Planes parallel to σ_2 with a pole between 17.0° and 13.8° with respect to σ_1 will be reactivated
	Planes parallel to σ_1 with a pole between 46.1° and 78.4° with respect to σ_2 will be reactivated
	Planes parallel to σ_3 with a pole between 7.8° and 23.0° with respect to σ_1 will be reactivated
F4	Planes parallel to σ_2 with a pole between 17.9° and 12.9° with respect to σ_1 will be reactivated
	Planes parallel to σ_1 with a pole between 41.5° and 79.4° with respect to σ_2 will be reactivated
	Planes parallel to σ_3 with a pole between 7.3° and 23.5° with respect to σ_1 will be reactivated

Fig. 18 Magnitude of the displacements (U is the resultant displacement of x and y directions) (m) in the geostatic step for F4. These displacements are very small, which confirms that the model is in geostatic equilibrium
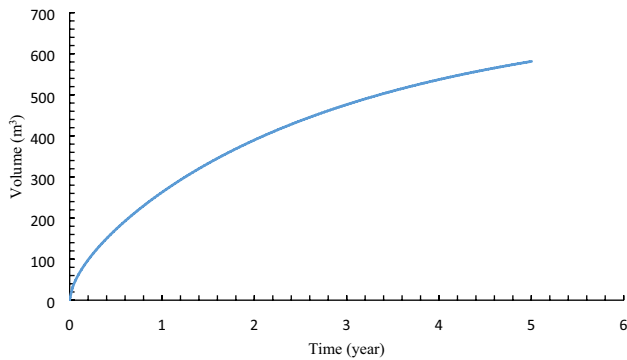

Fig. 19 Volume of the injected gas is about 581.5 m³ after 5 years for injection pressure of 30 MPa

located near the fault plane, which is another proof for this claim. By increasing the injection pressure up to 60 MPa, the slip and resulting strains initiated after 12 days of injection. Also at this injection pressure, plastic strains developed at the reservoir-cap rock interface due to the accumulation of high pore pressure in this area (Fig. 30).

Finally, the effect of the friction angle on fault stability was examined by reducing the coefficient of sliding friction to 0.4 at an injection pressure of 60 MPa. The injection continued until the slip and the consequent plastic strains initiated. Figure 31 shows the magnitude of plastic strains
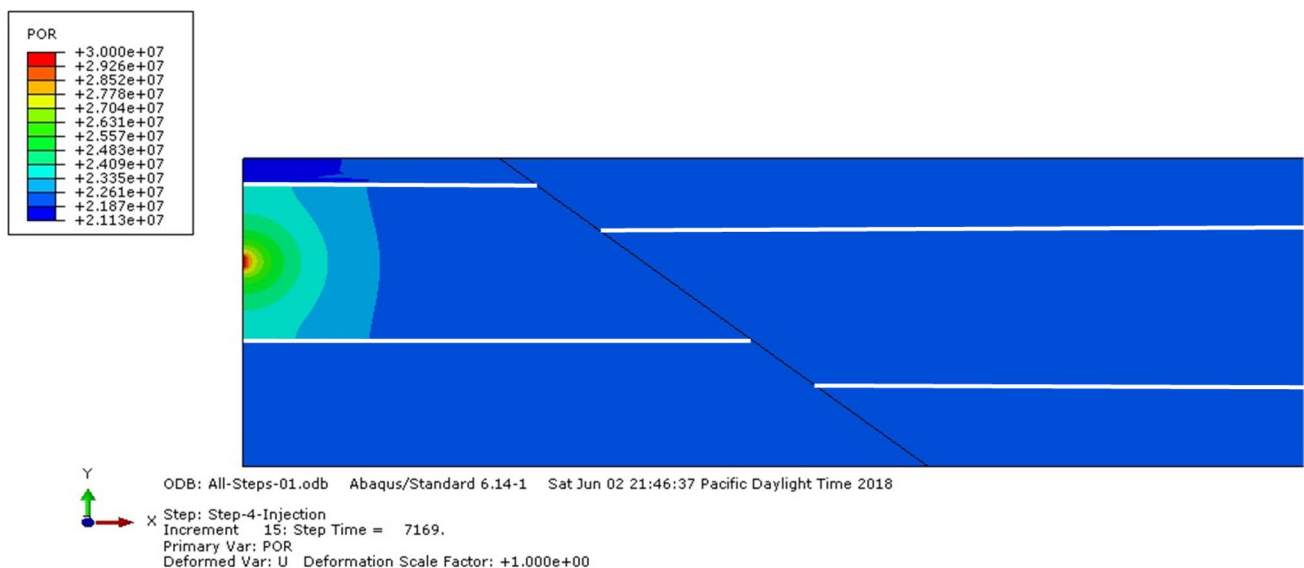
Fig. 20 Progression of the injected gas plume in the reservoir after two hours of injection (pore pressure in Pa). After 2 h, the gas plume has travelled about 150 m away from the injection point in the reservoir
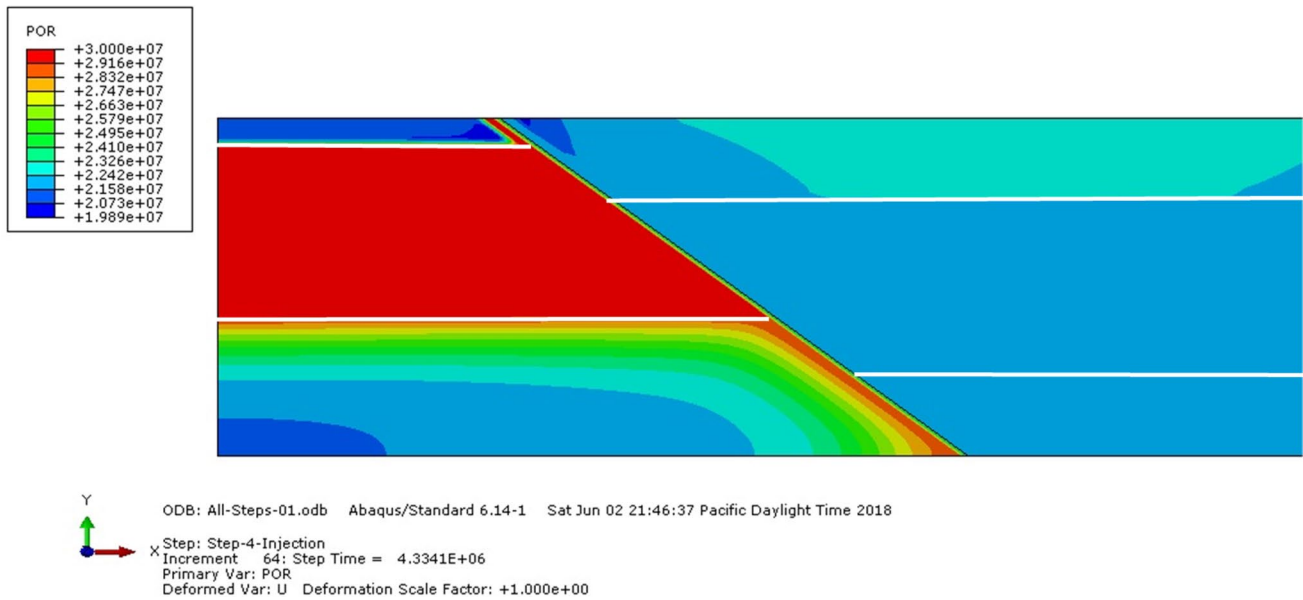
Fig. 21 Pore pressure build up through fault damage zone into Pabdeh source rock. Due to the higher permeability of the damage zone, the pore pressure plume first penetrates the Pabdeh source rock, and at the end of 5 years, it also infiltrates the cap rock (pore pressure in Pa). Furthermore, the ascending gasses from the reservoir-cap rock interface slightly infiltrate the lower part of the cap rock
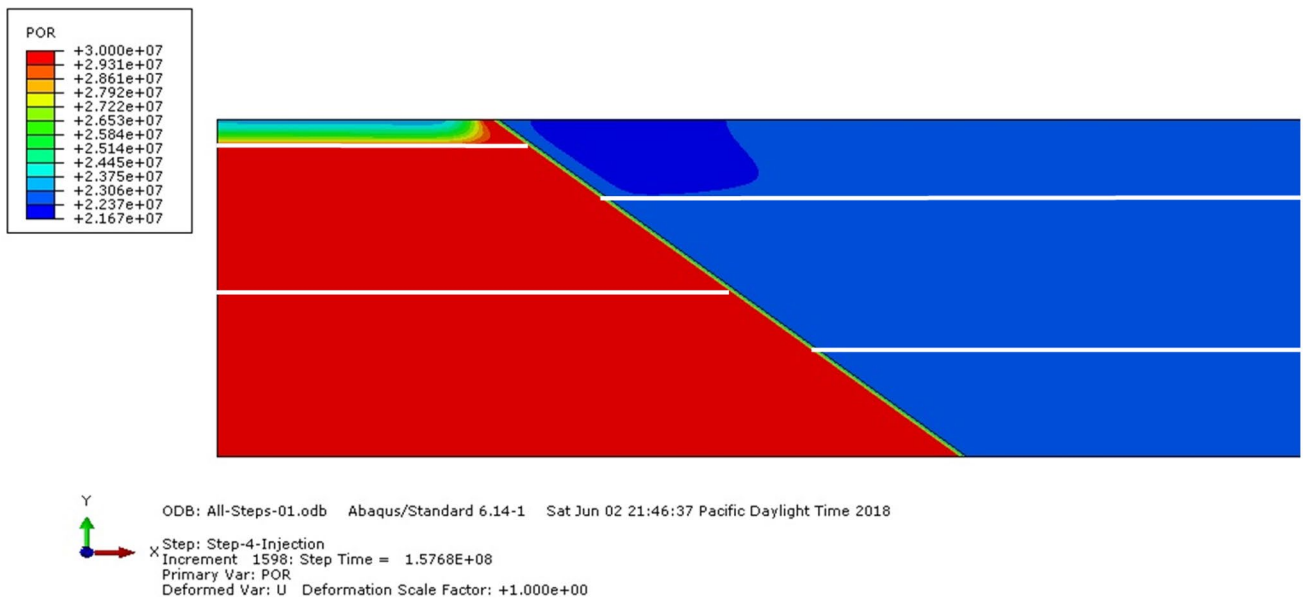

Fig. 22 Pore pressure increase (Pa) in the injected block. At the end of the 5 years, some parts of the cap rock have experienced pore pressure increase due to the moving gas from both the damage zone and reservoir-cap rock interface. At the same time, the other side of the fault has undergone a little change, since the fault core acts as a barrier and hinders the gas from moving forward

for different frictional coefficients at injection pressure of 60 MPa. For the injection with $\mu = 0.6$, the first plastic strains appeared after 12 days. By reducing μ to 0.4, the slip initiated only after 10 days of injection. It can also be inferred that by reducing μ, the accumulated plastic strain decreases, since the two blocks of rocks can slide more easily. These results indicate that the role of the frictional
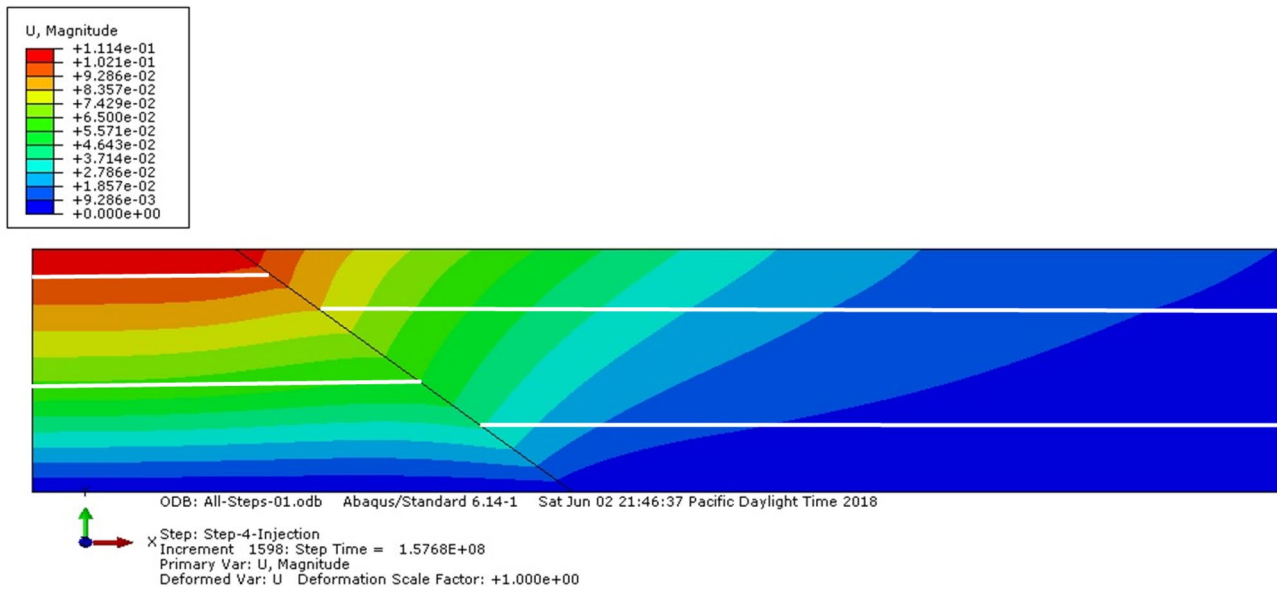
Fig. 23 Contours of displacement (m) over the injected area. The maximum induced uplift is about 11 cm above the injection area. This uplift is mainly because of reservoir compartmentalization by

the impermeable fault core, which has trapped the gas in the injected block (left side of the fault)
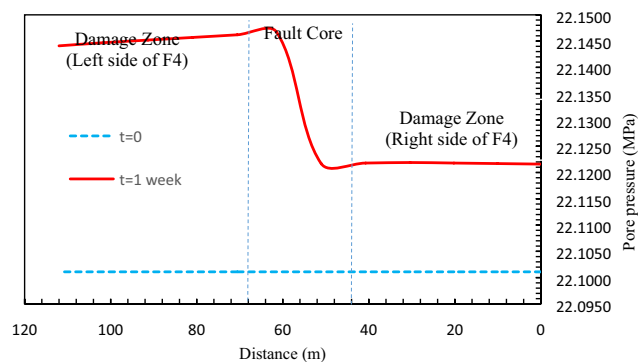
Fig. 24 Pore pressure increase for a path perpendicular to F4, at the beginning and 1 week after injection. The impermeable fault core acts as a barrier and prevents the gas plume from spreading

coefficient on fault stability can be more influential than injection pressure.

5 Conclusions

In this study, a step by step procedure was followed to investigate the stability of four faults in Asmari reservoir, Gachsaran oilfield, SW Iran. To achieve this goal, the current stress field was determined using well logs and poroelastic equations. The field is in a normal faulting stress regime, which is confirmed by the presence of normal faults that cut the lower parts of the cap rock. By
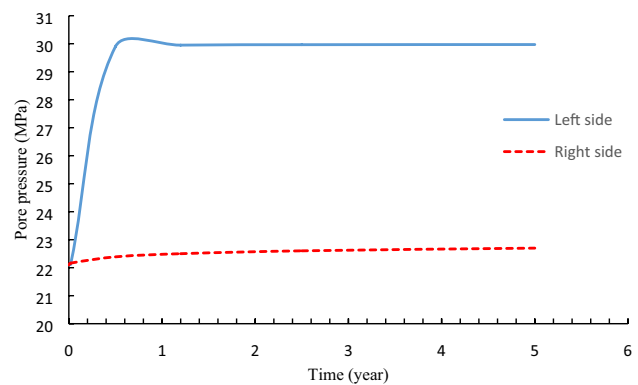

Fig. 25 Pore pressure variations over time for two elements on the sides of F4. The pore pressure on the left side of the fault reaches 30 MPa after 6 months, but on the right side, it rises only about 0.5 MPa after 5 years

plotting Mohr diagrams, it was demonstrated that all the faults are stable in the current stress field and pore pressure. Mohr diagrams were also used to estimate the maximum sustainable pore pressure and the creation of new fractures. According to these analytical results, the most stable fault in the field is F2 which can support maximum pore pressures of 55–57 MPa. F3 was recognized to be the most prone to reactivation ($P_{pmax} = 38.8$ MPa). This low value may, however, be due to the short length of this fault within the reservoir and the numerical generation of anomalously large amounts of shear stress on the
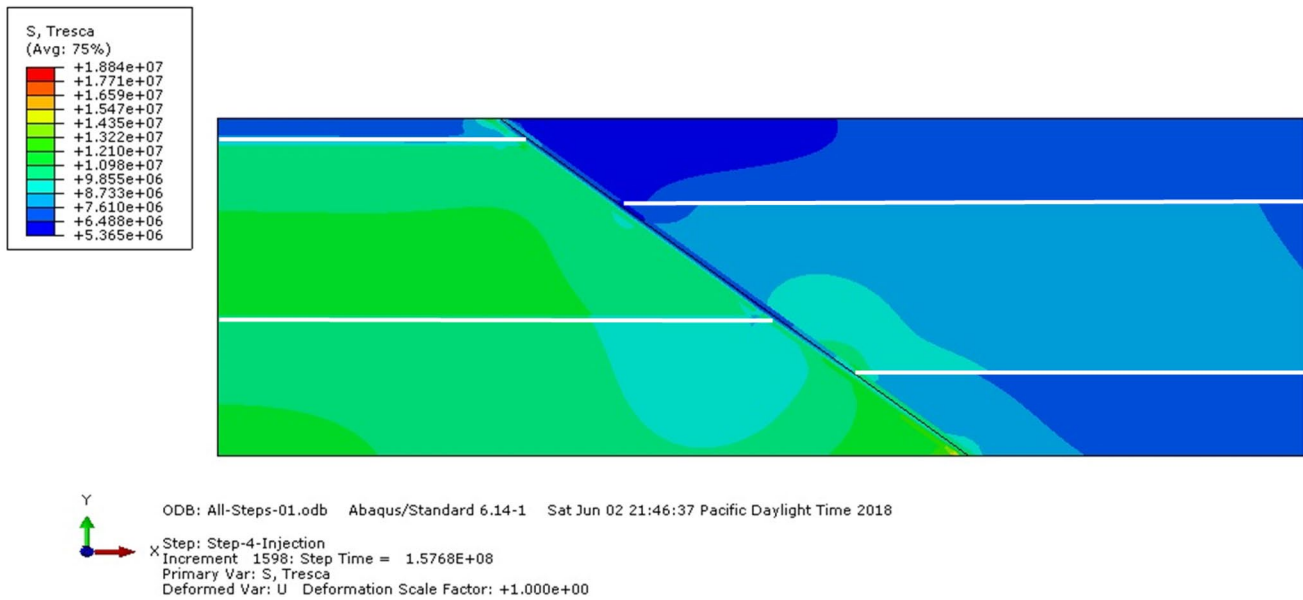
Fig. 26 Maximum shear stress accumulated on F4 is about 13 MPa after 5 years of injection. This stress is mainly accumulated in the injected block (left side). The accumulation and distribution of this shear stress will be the main reason of plastic strain growth and fault reactivation with higher injection pressures
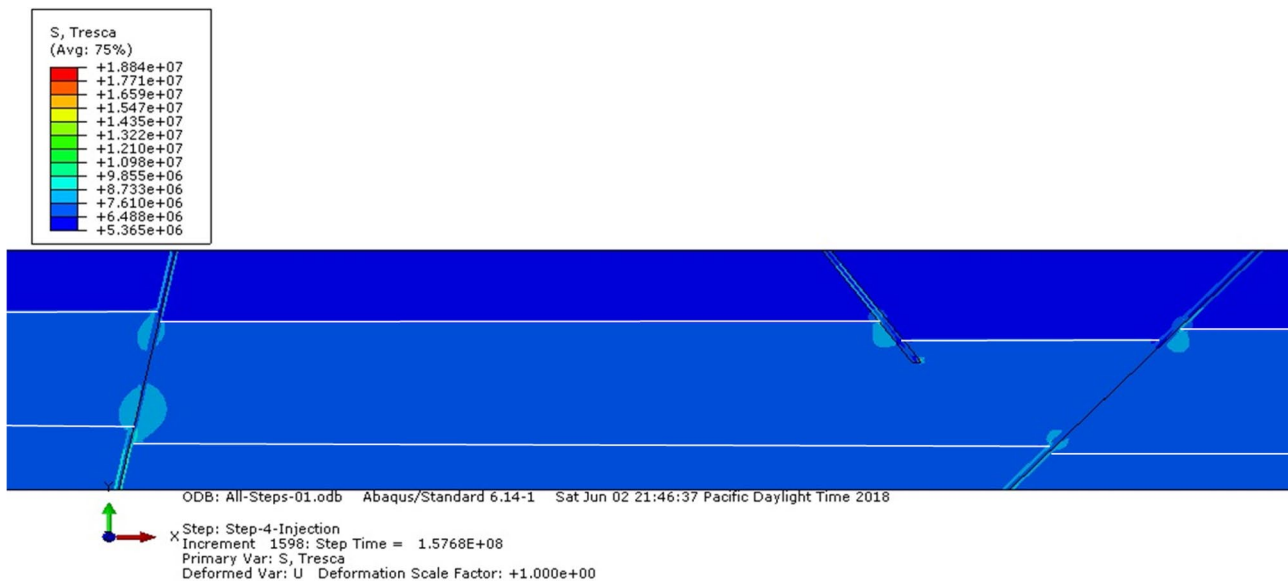

Fig. 27 Maximum shear stress accumulated on F1, F2, and F3 is about 8 MPa after 5 years of injection. The magnitude of shear stress for these faults have not increased as much as for F4, since these areas have not experienced equal pore pressure increase due to F4 impermeability

small fault segment. By comparing the injection pressures needed to create fractures in intact rocks around each fault, it was also recognized that the reservoir could be divided into two regions of low strength (west to southwest) and higher strength (northwest).

Numerical simulations were carried out to investigate the potential fluid flow, fault reactivation, and propagation of shear stress and plastic strain in different parts of the reservoir. A pressure of 30 MPa was recognized as the safe lower bound of injection pressure, since it did not induce hydraulic fractures or cause fault slip. Due to fault compartmentalization, the simulated injection resulted in overpressures leading to an uplift of about 11 cm at the end of 5 years. An increase in injection pressure up to 50 MPa and 60 MPa leads to fault slip in 100 and 12 days, respectively. For an injection pressure of 60 MPa, the onset of
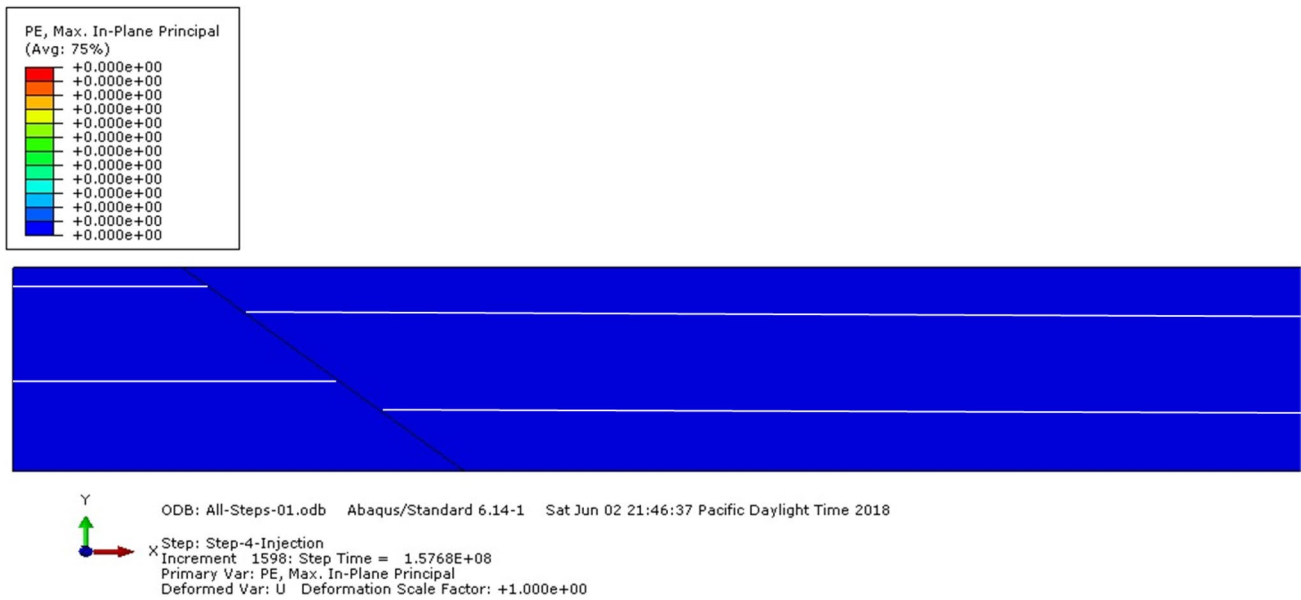
Fig. 28 No plastic strain was formed over time in the reservoir or cap rock for the injection pressure of 30 MPa. This implies that this pressure is safe for the reservoir, and cap rock integrity is not compromised
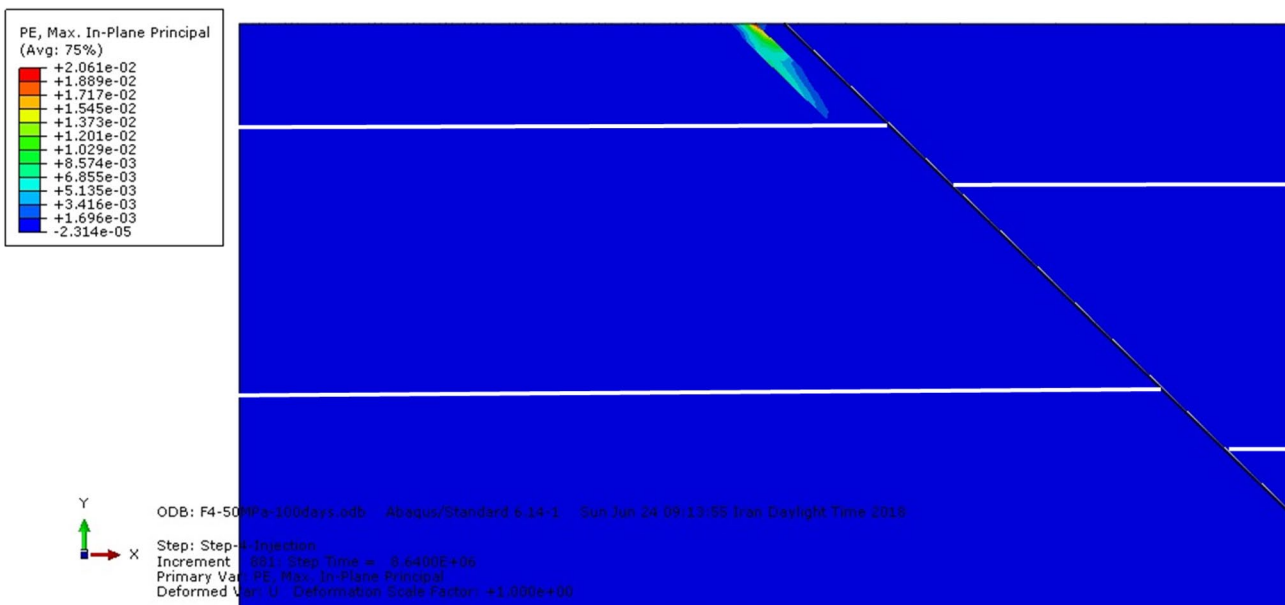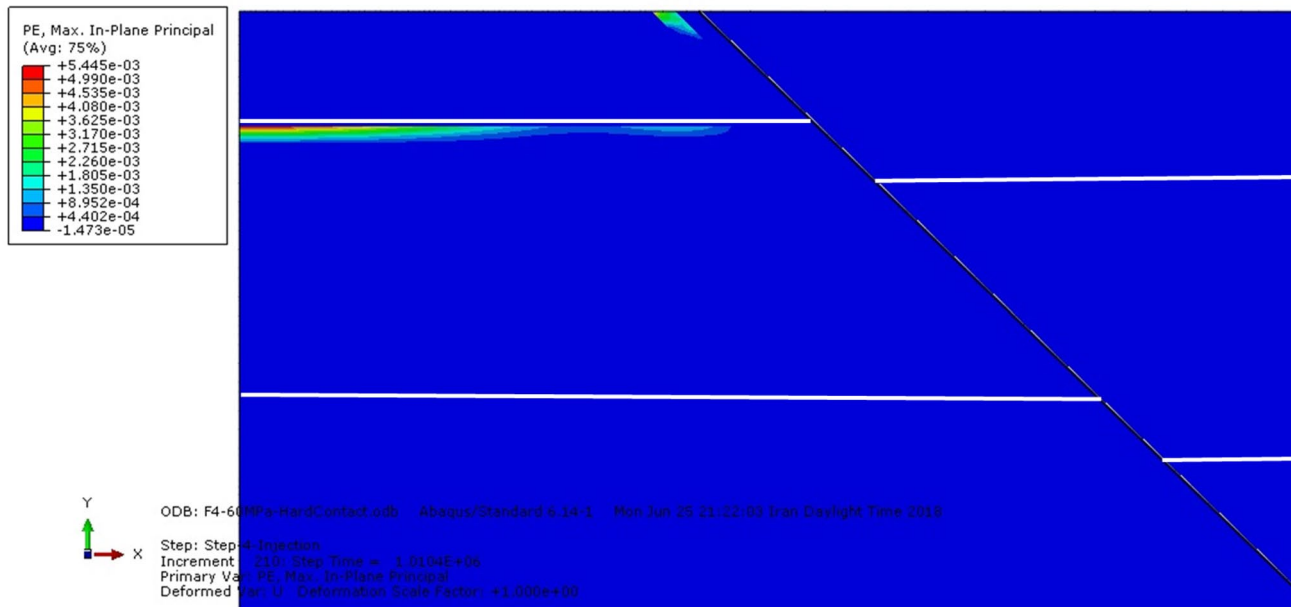

Fig. 29 Onset of plastic strains at the fault plane in the cap rock after 100 days of injection with an injection pressure of 50 MPa. These strains indicate the onset of fault reactivation and end of simulation

reactivation occurred earlier by reducing the frictional coefficient value from 0.6 to 0.4.

The results of both analytical methods and numerical simulations are consistent with each other and suggest an approximate safe injection pressure range of 30–50 MPa. One of the main uncertainties related to analytical methods is reservoir-cap rock system properties such as permeability, which plays a significant role in the injected gas flow

Fig. 30 Onset of plastic strains at the fault plane and reservoir-cap rock interface (caused by ascending gasses) after 12 days of injection with an injection pressure of 60 MPa
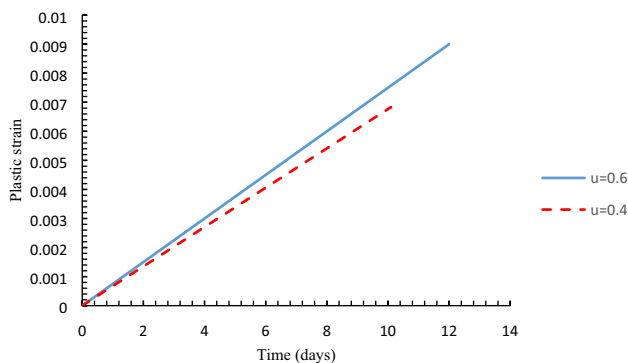
Fig. 31 Onset of plastic strain for frictional coefficients of $\mu = 0.6$ and $\mu = 0.4$ at the injection pressure of 60 MPa. By reducing the frictional coefficient, the slip initiated in 10 days. For $\mu = 0.4$ the accumulated plastic strain decreases, since the two blocks of rocks can slide easier

pattern and imposing the location of accumulated plastic strains.

Compliance with Ethical Standards

References

Alizadeh B, Maroufi K, Fajrak M (2018) Hydrocarbon reserves of Gachsaran oilfield, SW Iran: geochemical characteristics and origin. Mar Pet Geol 92:308–318

Alizadeh M, Movahed Z, Junin R, Mohsin R, Alizadeh M, Alizadeh M (2015) Finding the drilling induced fractures and borehole breakouts directions using image logs. J Adv Res Appl Mech 1:9–30

Allmendinger RW (2017) A structural geology laboratory manual for the 21st century. http://www.geo.cornell.edu/geology/faculty/RWA/structure-lab-manual/. Accessed 24 June 2018

Anderson EM (1951) The dynamics of faulting and dyke formation with applications to Britain. Oliver and Boyd, Edinburgh

Asquith G, Krygowski D, Gibson C (2004) Basic well log analysis 16. American Association of Petroleum Geologists, Tulsa

Azadpour M, Shad Manaman N, Kadkhodaie-Ilkhchi A, Sedghipour MR (2015) Pore pressure prediction and modeling using well-logging data in one of the gas fields in south of Iran. J Pet Sci Eng 128:15–23

Barton CA, Zoback MD, Moos D (1995) Fluid flow along potentially active faults in crystalline rock. Geology 23:683–686

Berberian M, King GCP (1981) Towards a paleogeography and tectonic evolution of Iran. Can J Earth Sci 18:210–265

Blanton TL, Olson JE (1999) Stress magnitudes from logs-effects of tectonic strains and temperature. SPE Res Eval Eng 2:62–68

Byerlee JD (1978) Friction of rock. Pure Appl Geophys 116:615–626

Caine JS, Evans JP, Foster CB (1996) Fault zone architecture and permeability structure. Geology 24:1025–1028

Carlsson A, Olsson T (1979) Hydraulic conductivity and its stress dependence. In: Proceedings, Paris, workshop on low-flow, low-permeability measurements in largely impermeable rocks, pp 249–259

Castelletto N, Gambolati G, Teatini P (2013) Geological CO_2 sequestration in multi-compartment reservoirs: geomechanical challenges. J Geophys Res Solid Earth 118:2417–2428

Chang C, Zoback MD, Khaksar A (2006) Empirical relations between rock strength and physical properties in sedimentary rocks. J Pet Sci Eng 51:223–237

Cornet FH (2012) The relationship between seismic and aseismic motions induced by forced fluid injections. Hydrogeol J 20:1463–1466

Crain ER (2017) Crain's petrophysical handbook—3rd Millennium edition, An internet-based worldwide e-learning project for petrophysics. http://ww.spec2000.net. Accessed 24 June 2018

Darvishzadeh A (2009) Geology of Iran: stratigraphy, tectonic, metamorphism, and magmatism. Amir Kabir Press, Tehran (**In Persian**))

Evans KF, Zappone A, Kraft T, Deichmann N, Moia F (2012) A survey of the induced seismic responses to fluid injection in geothermal and CO_2 reservoirs in Europe. Geothermics 41:30–54

Ferrill DA, Morris AP (2003) Dilational normal faults. J Struct Geol 25:183–196

Ferrill DA, Winterle J, Wittmeyer G, Sims D, Colton S, Armstrong A (1999) Stressed rock strains groundwater at Yucca Mountain, Nevada. GSA Today 9:1–8

Ferrill DA, Smart KJ, Morris AP (2019) Fault failure modes, deformation mechanisms, dilation tendency, slip tendency, and conduits versus seals. Geol Soc Lond Spec Publ. https://doi.org/10.1144/SP496-2019-7

Figueiredo B, Tsang CF, Rutqvist J, Bensabat J, Niemi A (2015) Coupled hydro-mechanical processes and fault reactivation induced by CO_2 injection in a three-layer storage formation. Int J Greenh Gas Control 39:432–448

Gartrell A, Bailey WR, Brincat M (2006) A new model for assessing trap integrity and oil preservation risks associated with post-rift fault reactivation in the Timor Sea. Am Assoc Pet Geol Bull 90:1921–1944

Geological Society of Iran, GSI (2018). http://www.geosociety.ir

Grosser BT (2012) fault and fracture reactivation in the Penola Trough, Otway Basin. Thesis submitted in accordance with the requirements of the University of Adelaide for an Honours Degree in Geology

Guha SK (2000) Induced earthquakes. Springer, Berlin

Hansen O, Gilding D, Nazarian B, Osdal B, Ringrose P, Kristoffersen JB, Eiken O, Hansen H (2013) Snohvit: the history of injecting and storing 1 Mt CO_2 in the Fluvial Tubaen Fm. Energy Procedia 37:3565–3573

Hawkes CD, Mclellan PJ, Bachu S (2005) Geomechanical factors affecting geological storage of CO_2 in depleted oil and gas reservoirs. J Can Pet Technol 44:52–61

Hillis RR (2001) Coupled changes in pore pressure and stress in oil fields and sedimentary basins. Pet Geosci 7:419–425

Ito T, Zoback MD (2000) Fracture permeability and in situ stress to 7 km depth in the KTB Scientific Drillhole. Geophys Res Lett 27:1045–1048

Jaeger JC, Cook NGW (1971) Fundamentals of rock mechanics. Chapman and Hall, London

Jaeger JC, Cook NGW, Zimmerman R (2009) Fundamentals of rock mechanics. Wiley, New York

James GA, Wynd JG (1965) Stratigraphic nomenclature of Iranian oil consortium agreement area. Am Assoc Petrol Geol Bull 49:2182–2245

Jeanne P, Guglielmi Y, Cappa F, Rinaldi AP (2014) Architectural characteristic and distribution of hydromechanical properties within a small strike-slip fault zone in carbonates reservoir: impact on fault stability, induced seismicity, and leakage during CO_2 injection. AGU Fall Meet. https://doi.org/10.13140/2.1.1060.7689

Jennings JW, Lucia FJ (2001) Predicting permeability from well logs in carbonates with a link to geology for interwell permeability mapping. In: SPE annual technical conference and exhibition

Jolie E, Moeck I, Faulds JE (2015) Quantitative structural-geological exploration of fault-controlled geothermal systems—a case study from the Basin-and-Range Province, Nevada (USA). Geothermics 54:54–67

Keranen KM, Savage HM, Abers GA, Cochran ES (2013) Potentially induced earthquakes in Oklahoma, USA: links between wastewater injection and the 2011 Mw 5.7 earthquake sequence. Geology 41:699–702

Konstantinovskaya E, Malo M, Castillo DA (2012) Present-day stress analysis of the St. Lawrence lowlands sedimentary basin (Canada) and implications for cap rock integrity during CO_2 injection operations. Tectonophysics 518–521:119–137

Kulikowski D, Amrouch K, Cooke D (2016) Geomechanical modelling of fault reactivation in the Cooper Basin, Australia. Aust J Earth Sci 63:295–314

Langhi L, Zhang Y, Gartrell A, Underschultz J, Dewhurst D (2010) Evaluating hydrocarbon trap integrity during fault reactivation using geomechanical three-dimensional modeling: an example from the Timor Sea, Australia. Am Assoc Petrol Geol Bull 94:567–591

Lucia FJ (2007) Carbonate reservoir characterization an integrated approach, 2nd edn. Springer, Berlin

McGarr A, Bekins B, Burkardt N, Dewey J, Earle P, Ellsworth W, Ge S, Hickman S, Holland A, Majer E, Rubinstein J, Sheehan A (2015) Coping with earthquakes induced by fluid injection. Science 347:830–831

Meng L, Fu X, Lv Y, Li X, Cheng Y, Li T, Jin Y (2016) Risking fault reactivation induced by gas injection into depleted reservoirs based on the heterogeneity of geomechanical properties of fault zones. Pet Geosci 23:29–38

Mildren SD, Hillis RR, Dewhurst DN, Lyon PJ, Meyer JJ, Boult PJ (2005) FAST: a new technique for geomechanical assessment of the risk of reactivation-related breach of fault seals. In: Boult P, Kaldi J (eds) Evaluating fault and cap rock seals 2. Proceedings of the AAPG Hedberg Conference, Barossa Valley, South Australia, Australia AAPG Heidelberg Series, pp 73–85

Moeck I, Kwiatek G, Zimmermann G (2009) Slip tendency analysis, fault reactivation potential and induced seismicity in a deep geothermal reservoir. J Struct Geol 31:1174–1182

Morris A, Ferrill DA, Brent Henderson DB (1996) Slip-tendency analysis and fault reactivation. Geology 24:275–278

Muvdi BB, McNabb JW (1991) Engineering mechanics of materials, 3rd edn. Springer, Berlin

Nacht PK, de Oliveira MFF, Roehl DM, Costa AM (2010) Investigation of geological fault reactivation and opening. de Mecanica Computacional 89:8687–8697

Nicholson C, Wesson RL (1990) Earthquake hazard associated with deep well injection. United States Geological Survey Bulletin, 1951

Plumb R (1994) Influence of composition and texture on the failure properties of clastic rocks. In: Rock mechanics in petroleum engineering, 29–31 August, Delft, Netherlands

Rezaee MR (2014) Petroleum geology. Alavi Press, Tehran (**in Persian**))

Rezaie AH, Nogole-Sadat MA (2004) Fracture modeling in Asmari reservoir of Rag-e Sefid oil field by using multiwall image log (FMS/FMI). Iran Int J Sci 5:107–121

Richey DJ (2013) Fault seal analysis for CO_2 storage: Fault zone architecture, fault permeability, and fluid migration pathways in exposed analogs in southeastern Utah. Ph.D. Thesis, Utah State University

Rutqvist J, Birkholzer J, Cappa F, Tsang CF (2007) Estimating maximum sustainable injection pressure during geological sequestration of CO_2 using coupled fluid flow and geomechanical fault-slip analysis. Energy Convers Manag 48:1798–1807

Rutqvist J, Tsang CF (2005) Coupled hydromechanical effects of CO_2 injection. In: Tsang CF, Apps JA (eds) Injections science and technology. Elsevier, Amsterdam, pp 649–679

Schmitt DR (2014) Basic geomechanics for induced seismicity: a tutorial. CSEG Rec 39:24–29

Shaban A, Sherkati S, Miri SA (2011) Comparison between curvature and 3D strain analysis methods for fracture predicting in the Gachsaran oilfield (Iran). Geol Mag 148:868–878

Sibson RH (1990) Faulting and fluid flow. In: Nerbitt BE (ed) Short course on fluids in tectonically active regions of the continental crust. Mineralogical Association of Canada Handbook, vol 18, pp 93–132

Sibson RH (1996) Structural permeability of fluid-driven fault-fracture. J Struct Geol 18:1031–1042

Siler D, Faulds J, Mayhew B, McNamara D (2016) Analysis of the favorability for geothermal fluid flow in 3D: Astor Pass geothermal prospect, Great Basin, Northwestern Nevada, USA. Geothermics 60:1–12

Stocklin J (1974) Possible ancient continental margin in Iran. In: Burk CA, Drake CL (eds) Geology of continental margins. Springer, Berlin, pp 873–887

Streit JE, Hillis RR (2004) Estimating fault stability and sustainable fluid pressures for underground storage of CO_2 in porous rock. Energy 29:1445–1456

Taghipour M, Ghafoori M, Lashkaripour GR, Hafezi Moghaddas N, Molaghab A (2019) Estimation of the current stress field and fault reactivation analysis in the Asmari reservoir, SW Iran. Pet Sci 16:513–526

Terzaghi K (1923) Die Berechning der Durchlässigkeitziffer des Tonesaus dem Verlauf Spannungserscheinungen, Akad. Der Wissenchafeb in Wien, Sitzungsberichte, Mathematisch-naturwissenschafttliche Klasse. Part lia 142(3/4):125–138

Verdon JP (2012) Microseismic monitoring and geomechanical modeling of CO_2 storage in subsurface reservoirs. Doctoral Thesis accepted by University of Bristol, United Kingdom, Springer Theses

Vilarrasa V, Makhnenko R, Gheibi S (2016) Geomechanical analysis of the influence of CO_2 injection location on fault stability. J Rock Mech Geotech Eng 8:805–818

Wiprut D, Zoback MD (2002) Fault reactivation, leakage potential, and hydrocarbon column heights in the northern North Sea. In: Koestler AG, Hunsdale R (eds) Hydrocarbon seal quantification, Norwegian Petroleum Society Conference, Stavanger, Norway, 16–18 October 2000. Norwegian Petroleum Society (NPF). Special publications, vol 11, pp 203–219

Yoon JS, Zang A, Stephansson O, Zimmermann G (2016) Modelling of fluid-injection-induced fault reactivation using a 2D discrete element based hydro-mechanical coupled dynamic simulator. Energy Procedia 97:454–461

Zang A, Stephansson O (2010) Stress field of the earth's crust. Springer, Berlin

Zhang MX, Lee XL, Javadi AA (2006) Behavior and fracture mechanism of brittle rock with pre-existing parallel cracks. Key Eng Mater 324–325:1055–1058

Zoback MD (2007) Reservoir geomechanics. Cambridge University Press, Cambridge

Zoback MD, Barton CA, Brudy M, Castillo DA, Finkbeiner T, Grollimund BR, Moos DB, Peska P, Ward CD, Wiprut DJ (2003) Determination of stress orientation and magnitude in deep wells. Int J Rock Mech Min Sci 40:1049–1076